JGR Earth Surface

RESEARCH ARTICLE
10.1029/2025JF008993

Local Characteristics of Sand Wave Patterns Are Governed by Underlying Sand Bank: A Linear Stability Approach

Laura Portos-Amill[1], Pieter C. Roos[1], Henk M. Schuttelaars[2], and Suzanne J. M. H. Hulscher[1]

[1]Water Engineering and Management, University of Twente, Enschede, the Netherlands, [2]Delft Institute of Applied Mathematics, Delft University of Technology, Delft, the Netherlands

Key Points:

- We extended a linear stability model to study sand wave formation on a sand bank characterized by a spatially non-uniform flow pattern
- The non-uniform sand bank topography and flow patterns trigger spatially confined eigenmodes reflecting local sand wave characteristics
- Our model reproduces local sand wave characteristics such as migration rate and orientation as observed on tidal sand banks

Correspondence to:
L. Portos-Amill,
l.portosamill@utwente.nl

Citation:
Portos-Amill, L., Roos, P. C., Schuttelaars, H. M., & Hulscher, S. J. M. H. (2026). Local characteristics of sand wave patterns are governed by underlying sand bank: A linear stability approach. *Journal of Geophysical Research: Earth Surface*, *131*, e2025JF008993. https://doi.org/10.1029/2025JF008993

Received 6 NOV 2025
Accepted 27 MAY 2026

Abstract Tidal sand waves are dynamic bedforms, observed in shelf seas. In some cases they co-exist with tidal sand banks, larger-scale bed features. Sand wave characteristics then vary over the sand bank, migrating anti-cyclonically around the bank. Yet, little is known about the processes behind sand wave formation on a sand bank characterized by a spatially non-uniform flow pattern. Here, we extend an existing linear stability model to assess the effects of an underlying sand bank on sand wave formation. Specifically, we allow for a spatially varying basic state, representing the topography of the bank as well as the typical 3D tidal and residual flow patterns over it. The eigenmodes of the system then turn out to be spatially varying too, that is, showing a sand wave pattern only on certain parts of the bank (trough, crest or one of the flanks). Therefore, sand wave characteristics across the sand bank are given by multiple modes, and not only by the fastest growing mode (FGM). This is a major difference with respect to previous studies, focusing on sand wave formation on a horizontal bed with a spatially uniform flow field. There, the pattern of each mode covered the entire domain, so the FGM was the single mode that represented the preferred sand wave pattern. Model results further show sand waves anti-cyclonically migrating around the sand bank, and crestline veering toward the sand bank crest. These results are in qualitative agreement with observations.

Plain Language Summary Different kinds of bedforms usually co-exist on tide-dominated seas, such as the North Sea. These include tidal sand waves and sand banks. Sand banks are several km long, around 10 m high and evolve at timescales of centuries to millennia. They are commonly covered by sand waves, smaller bedforms which are more dynamic, with wavelengths of hundreds of meters, heights of several meters and migration rates of around $1 - 10$ m/yr. Here we focus on how the static sand bank topography affects the superimposed and dynamic sand waves. To do so, we use a linear stability analysis and assume that sand waves form as growing topography perturbations on the sand bank. Previous linear stability analysis studies only considered a flat bed, but the addition of the background sand bank makes the results less straightforward. Results on a flat bed yield sand wave perturbations that are uniform in space, covering the entire domain and characterized by a single growth and migration rates. Differently, the non-uniform sand bank topography and associated flow patterns make the sand wave perturbations to be spatially confined. Thus a single perturbation cannot explain sand wave formation across the sand bank, but several perturbations must be considered.

1. Introduction

The seabed of shallow tide-dominated seas is usually covered by dynamic bedforms such as tidal sand waves and tidal sand banks, among others (Figure 1). Sand waves are usually characterized by wavelengths of several hundreds of meters, heights of $1 - 10$ m, migration rates of $1 - 10$ m yr^{-1}, and their crests are typically parallel to the main tidal flow direction (van der Meijden et al., 2023; van Dijk & Kleinhans, 2005). A better understanding of the evolution of sand waves is needed because, for example, as they migrate, they may expose buried cables or pipelines, or they may interfere with navigation (Németh et al., 2003).

Sand waves are often found to co-exist with sand banks. Here, we will focus on the influences of an underlying sand bank on sand wave characteristics. Sand banks are typically larger than sand waves, with wavelengths on the order of around 10 km and heights on the order of 10 m. From the perspective of sand waves, sand banks may be considered static bedforms given that they evolve on timescales of centuries to millennia and display almost no migration. Sand banks are often elongated and cyclonically oriented with respect to the main direction of the tidal flow (de Swart & Yuan, 2019). Examples of seas where sand waves and sand banks co-exist include the Dutch

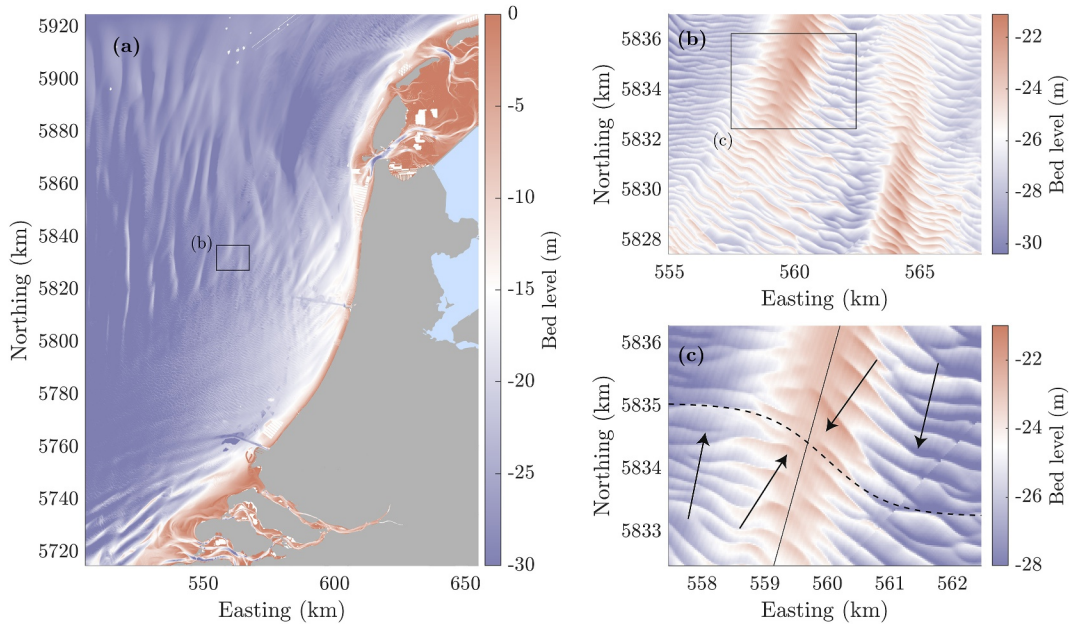

Figure 1. Panel (a): Bathymetric chart of the Netherlands Continental Shelf. Panels (b and c) show details of sand waves on a sand bank. The dashed line in panel (c) highlights how the sand wave crest orientation changes across a sand bank; the solid line indicates the bank crest. The arrows in panel (c) denote the direction of sand wave migration, showing veering toward the sand bank crest (migration direction taken from van der Meijden et al. (2023)). Note the different spatial scales. Data from the Netherlands Hydrographic Service.

North Sea (van der Spek et al., 2022), the South China Sea (Zhou et al., 2022), and the Irish Sea (van Landeghem et al., 2012).

So far, sand wave formation studies have mainly focused on the case with a horizontal background topography. Hulscher (1996) first explained sand wave formation as an inherent instability of a flat sandy seabed subject to tidal flow using a linear stability analysis of an idealized process-based model. Note that a linear stability analysis can only give information on the initial stage of sand wave formation, where nonlinear interactions are negligible. Still, the obtained values for preferred wavelength and migration rate tend to agree with those observed on a horizontal seabed (Dodd et al., 2003). In follow-up studies, the work of Hulscher (1996) was expanded to further include sand wave migration (e.g., Besio et al., 2008; Németh et al., 2002).

However, the modeling approach above is not suited for sand wave patterns on a sand bank because sand wave characteristics are observed to depend on the local background topography, for example, the crest, trough, or flanks of a sand bank. Specifically, sand waves are observed to be more three-dimensional on the bank flanks (Krabbendam et al., 2023), to migrate anti-cyclonically and slightly uphill around the sand bank (Caston, 1972; Zhou et al., 2022), and to veer toward the sand bank crest as they migrate (Caston & Stride, 1970). This is due to how local hydrodynamics are affected by a sand bank, including the deflection of the tidal ellipse and the generation of an anti-cyclonic residual circulation around a sand bank (Caston & Stride, 1970; Huthnance, 1973). Furthermore, van Landeghem et al. (2012) and Ma et al. (2018) observed faster sand wave migration in the vicinity of a sand bank, likely to be caused by the sand bank-induced deflection of currents.

Some morphodynamic modeling studies have addressed the co-existence of sand banks and sand waves. For example, Komarova and Newell (2000) argued that sand banks emerge from the nonlinear coupling among sand waves with different topographic wave numbers. Sand wave migration was, however, not included in the model, even though it is an essential trait of sand waves on sand banks. Recently, the numerical study by Leenders et al. (2021) quantified the cross-bank sediment transport direction over a single, externally imposed sand wavefield on a sand bank, both treated as morphostatic. Model results show upslope cross-bank sediment transport, potentially explaining sand bank growth. However, by fixing the wavelength and orientation of the sand wavefield, their approach did not allow for self-organization into a preferred sand wave pattern. Using a numerical model, Krabbendam et al. (2023) successfully reproduced the more three-dimensional character of sand

wave fields on the flanks of several sand banks on the Netherlands Continental Shelf. However, this computationally heavy approach did not systematically study the characteristics of the modes governing the sand wave formation stage nor the mechanisms involved.

From the literature review above, we conclude that there is not yet a 3D model able to represent the initial stage of sand wave formation on an underlying sand bank. Therefore, the aim of this study is to understand how sand wave characteristics (wavelength, orientation and migration rate) are locally affected by an underlying sand bank topography and associated flow patterns during the initial formation stage. To this end, we extend previous linear stability models (e.g., Hulscher, 1996) to incorporate a non-horizontal background topography, in this case a sand bank, and associated flow patterns. Specifically, we consider a static sand bank with an along-bank uniform topography and an idealized cross-bank profile. We impose the depth-averaged components of the residual and semi-diurnal tidal flow based on both observations (Caston & Stride, 1970; Huthnance, 1973) and modeling studies (Loder, 1980; Loder & Wright, 1985; van den Eynde et al., 2010) so as to represent the residual circulation around the sand bank and the veering of the tidal ellipse. A linear stability analysis then reveals the type of sand wave patterns that tend to form on the various parts of the sand bank (crest, trough, flanks).

This study is the first of its kind, performing a linear stability analysis on a sand bank characterized by a spatially non-uniform flow pattern. The system dynamics are governed by a 3D model, unraveling the differences that arise with respect to the horizontal case. One fundamental difference with respect to the horizontal case is that the sand wave shape in the cross-bank direction cannot be assumed a priori, therefore requiring a numerical discretization in the cross-bank direction. Methodologically, our study bears similarity with the model studies of shoreface-connected ridge formation by Trowbridge (1995) and Calvete et al. (2001). However, those studies adopted a depth-averaged flow model.

This paper is organized as follows. In Section 2, the process-based morphodynamic model is presented, capturing the 3D flow and sediment transport over the sand bank and the superimposed sand wave patterns. Then, Section 3 contains the full solution method, describing how the basic state and the perturbed state are solved. Results are presented in Section 4 and discussed in Section 5. Section 6 contains the conclusions.

2. Model Formulation

Consider an offshore region of a tide-dominated sea, covered by elongated sand banks, well away from coastal boundaries. We use a 3D Cartesian coordinate system with horizontal coordinates x^*, y^* in the along- and cross-bank directions, respectively (Figures 2a and 2b). The vertical coordinate, z^*, points upward, with $z^* = 0$ representing the undisturbed water level (Figure 2c). The sea surface elevation is denoted by $z^* = \zeta^*(x^*, y^*, t^*)$, with time t^*, and the bed level by $z^* = -H^*(y^*) + h^*(x^*, y^*, t^*)$, distinguishing two contributions: the sand bank topography, $H^*(y^*)$, is assumed static and uniform in the along-bank direction; while the overlying sand wave topography, $h^*(x^*, y^*, t^*)$, depends on both horizontal coordinates and is time-dependent. Velocities in the x^*, y^*, z^* directions are denoted by $u^*(x^*, y^*, z^*, t^*), v^*(x^*, y^*, z^*, t^*)$ and $w^*(x^*, y^*, z^*, t^*)$, respectively.

We use an idealized sand bank topography (Figure 2b), defined as

$$H^*(y^*) = H_0^* - H_{sb}^* \left(\frac{1}{2} - \frac{1}{2} \cos\left(\frac{2\pi y^*}{L_{dom}^*} \right) \right)^n, \quad \text{for } 0 \leq y^* < L_{dom}^*, \tag{1}$$

where H_0^* denotes the ambient depth, H_{sb}^* denotes the sand bank height, L_{dom}^* denotes the cross-bank domain size, and the exponent n controls the sand bank width and steepness. Our choice of $L_{dom}^* = 35$ km and $n = 10$ yields a sand bank width of roughly 15 km. We assume the sand bank topography to be spatially periodic in y^*, and so are the sand waves on top.

Flow is described by the 3D shallow water equations, given by

$$\frac{\partial u^*}{\partial t^*} + u^* \frac{\partial u^*}{\partial x^*} + v^* \frac{\partial u^*}{\partial y^*} + w^* \frac{\partial u^*}{\partial z^*} - f^* v^* = -F^* - g^* \frac{\partial \zeta^*}{\partial x^*} + A_v^* \frac{\partial^2 u^*}{\partial z^{*2}}, \tag{2a}$$

$$\frac{\partial v^*}{\partial t^*} + u^* \frac{\partial v^*}{\partial x^*} + v^* \frac{\partial v^*}{\partial y^*} + w^* \frac{\partial v^*}{\partial z^*} + f^* u^* = -G^* - g^* \frac{\partial \zeta^*}{\partial y^*} + A_v^* \frac{\partial^2 v^*}{\partial z^{*2}}, \tag{2b}$$

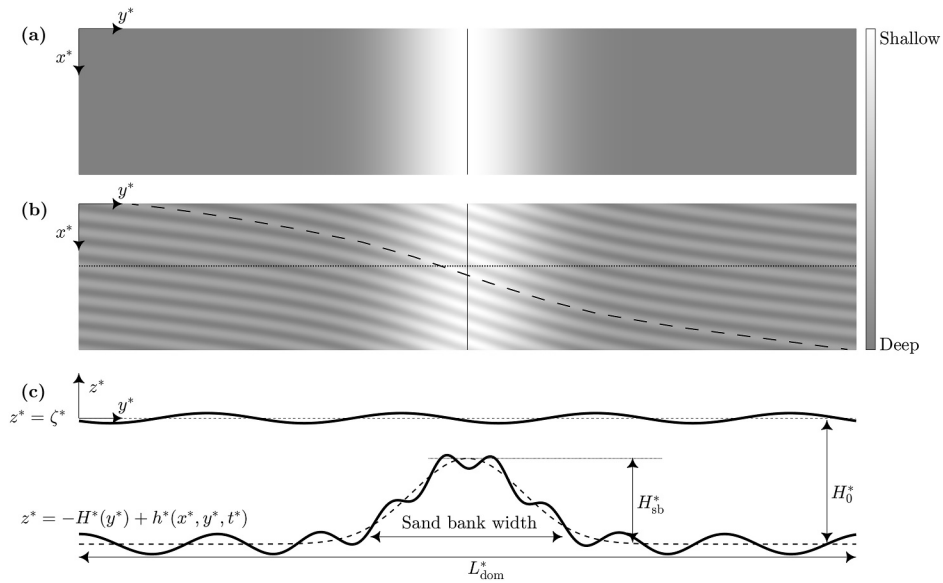

Figure 2. Definition sketch of model domain: (a) top view of the sand bank background topography, (b) top view of a sand wavefield on the underlying sand bank, (c) side view showing the sand bank profile according to Equation 1 (dashed line) and the superimposed sand wave field, as well as the associated sea surface elevation (solid lines). The solid lines in panels (a) and (b) denote the sand bank crest. The dashed line in panel (b) highlights how the sand wave crest orientation changes across a sand bank. The dotted line in panel (b) shows the along-bank location for which the transect in panel (c) is shown.

$$\frac{\partial u^*}{\partial x^*} + \frac{\partial v^*}{\partial y^*} + \frac{\partial w^*}{\partial z^*} = 0, \tag{2c}$$

where $f^* = 2\Omega^* \sin\vartheta$ is the Coriolis parameter (with $\Omega^* = 7.292 \cdot 10^{-5}$ rad s^{-1} the angular frequency of the Earth's rotation and ϑ the latitude), g^* is the gravitational acceleration, and A^*_v is the vertical eddy viscosity, assumed constant in time and uniform in space. The barotropic pressure gradient is decomposed into two components. The first part, F^*, G^*, is the sand bank-scale component, which effectively acts as a forcing term, prescribed such that a realistic depth-averaged tidal and residual flow pattern is obtained over the sand bank in the absence of sand waves (Section 3.3). The second component, $g^*\nabla^*_h\zeta^*$, is the pressure gradient, dynamically related to the presence of sand waves. Here, $\nabla^*_h = (\partial/\partial x^*, \partial/\partial y^*)$ denotes the horizontal nabla operator.

The hydrodynamic equations are supplemented with appropriate dynamic and kinematic boundary conditions. Specifically, at the sea surface, we impose zero shear stress for the horizontal velocities, while the condition for w^* is obtained by requiring the particles to follow the water surface. These conditions read

$$A^*_v\frac{\partial u^*}{\partial z^*} = A^*_v\frac{\partial v^*}{\partial z^*} = 0, w^* = \frac{\partial \zeta^*}{\partial t^*} + u^*\frac{\partial \zeta^*}{\partial x^*} + v^*\frac{\partial \zeta^*}{\partial y^*} \quad \text{at } z^* = \zeta^*. \tag{3}$$

At the seabed we impose a partial slip condition similar to Hulscher (1996), with slip parameter s^* being constant in time and uniform in space, for the horizontal velocities. The kinematic condition yields a constraint for w^* at the seabed, making particles follow the seabed surface:

$$\boldsymbol{\tau}^*_b \equiv A^*_v\frac{\partial \boldsymbol{u}^*}{\partial z^*} = s^*\boldsymbol{u}^*, w^* = u^*\frac{\partial z^*}{\partial x^*} + v^*\frac{\partial z^*}{\partial y^*} \quad \text{at } z^* = -H^* + h^*, \tag{4}$$

where $\boldsymbol{\tau}^*_b$ is the (volumetric) bed shear stress vector, and $\boldsymbol{u}^*$ is the velocity vector.

Sediment transport over sand banks and sand waves mainly occurs as bed load (Dyer & Huntley, 1999). Based on van Rijn (1993), the volumetric sediment transport is described by the following general transport formula:

$$\boldsymbol{q}_{\mathrm{b}}^{*}=\alpha^{*}|\boldsymbol{\tau}_{\mathrm{b}}^{*}|^{3/2}\left(\frac{\boldsymbol{\tau}_{\mathrm{b}}^{*}}{|\boldsymbol{\tau}_{\mathrm{b}}^{*}|}-\lambda^{*}\nabla_{\mathrm{h}}^{*}(-H^{*}+h^{*})\right)-\boldsymbol{q}_{\mathrm{b,bank}}^{*}, \tag{5}$$

where α^{*} is a bed load transport coefficient and λ^{*} is a bed slope correction parameter.

Given that sand waves evolve on a shorter timescale (order of several years) than sand banks (order of centuries to millennia), we consider a static sand bank. Therefore, we have added the contribution $-\boldsymbol{q}_{\mathrm{b,bank}}^{*}$ in Equation 5, which compensates the nonzero divergence of sediment transport that the model would yield over a sand bank and ensures the prescribed bank to be static. Physically, this term represents the mechanisms known to contribute to sand bank equilibria (e.g., wave stirring; see Roos et al., 2004) but are not included in this sand wave model. Consequently, a nonzero divergence of sediment transport, and thus bed evolution, exists only in the presence of sand waves. This is a similar approach to that followed by Calvete et al. (2001) in their study of shoreface connected ridge formation on a sloping shelf, precluding any morphodynamic evolution of the shelf itself. The added term $\boldsymbol{q}_{\mathrm{b,bank}}^{*}$ will be further specified in Section 3.3.

Bed evolution is modeled with the Exner equation,

$$\frac{\partial h^{*}}{\partial t^{*}}=-\frac{1}{1-\epsilon_{p}}\nabla_{\mathrm{h}}^{*}\cdot\boldsymbol{q}_{\mathrm{b}}^{*}, \tag{6}$$

where ϵ_{p} denotes sediment porosity.

3. Solution Method

3.1. Scaling Procedure

We scale the model equations in order to find the dominant balances and, if possible, to simplify the equations in a systematic way. To this end, we define the dimensionless quantities

$$\begin{gathered}
x=x^{*}/L^{*},\quad y=y^{*}/L^{*},\quad z=z^{*}/{H_{0}}^{*},\quad t=t^{*}\sigma^{*},\quad \tau=t^{*}/{T_{\mathrm{mor}}}^{*},\\
h=h^{*}/{H_{0}}^{*},\quad \zeta=\zeta^{*}g^{*}/U^{*2},u=u^{*}/U^{*},\quad v=v^{*}/U^{*},\quad w={w}^{*}\frac{L^{*}}{U^{*}H_{0}^{*}},\\
\boldsymbol{q}_{\mathrm{b}}=\frac{\boldsymbol{q}_{\mathrm{b}}^{*}}{\alpha^{*}\left(H_{0}^{*}U^{*}\sigma^{*}\right)^{3/2}},\quad \boldsymbol{\tau}_{\mathrm{b}}=\frac{\boldsymbol{\tau}_{\mathrm{b}}^{*}}{U^{*}H_{0}^{*}\sigma^{*}},\\
f=f^{*}/\sigma^{*},\quad F=F^{*}L^{*}/U^{*2},\quad G=G^{*}L^{*}/U^{*2},\\
A_{\mathrm{v}}={A_{\mathrm{v}}}^{*}/(\sigma^{*}H_{0}^{*,2}),\quad s=s^{*}/\left(H_{0}^{*}\sigma^{*}\right),\quad \lambda=\lambda^{*}{H_{0}}^{*}/L^{*},\\
\boldsymbol{q}_{\mathrm{b,bank}}=\frac{\boldsymbol{q}_{\mathrm{b,bank}}^{*}}{\alpha^{*}\left(H_{0}^{*}U^{*}\sigma^{*}\right)^{3/2}}.
\end{gathered} \tag{7}$$

An overview of model parameters and their default values is given in Table 1. Here, H_{0}^{*} is the vertical length scale and U^{*} is the scale for the horizontal velocity. We define the horizontal length scale L^{*} as the tidal excursion length, $L^{*}=U^{*}/\sigma^{*}$, with σ^{*} the angular frequency of the semidiurnal lunar tidal constituent (M2). We scale time against the hydrodynamic timescale, $T_{\mathrm{M2}}^{*}=2\pi/\sigma^{*}\sim 12$ hr, and we treat the hydrodynamic forcing and solution as the sum of tidal constituents,

$$u(x,y,z,t)=\sum_{p=-P}^{+P}U_{p}(x,y,z)\exp(ipt). \tag{8}$$

Here, P is the tidal constituent at which the solution is truncated. Similar expressions follow for v,w, and for $F,G,\zeta,\boldsymbol{q}_{\mathrm{b}}$ (omitting the z dependence).

Table 1
Overview of Model Parameters, Their Default Values and Units

Symbol	Name	Default value and units
U^*	Horizontal velocity scale	0.7 m s^{-1}
T^*_{M2}	M2 tidal period	12 hr 25 min 12 s
σ^*	M2 angular frequency	$1.4 \cdot 10^{-4}$ s^{-1}
L^*	Horizontal length scale	5 km
H^*_0	Ambient water depth (serving as vertical length scale)	25 m
ϵ_p	Sediment porosity	0.4 (−)
α^*	Bed load coefficient	0.51 $m^{-1}s^2$
Ω	Angular frequency of Earth's rotation	$7.2921 \cdot 10^{-5}$ s^{-1}
ϑ	Latitude	52°N
f^*	Coriolis parameter	$1.15 \cdot 10^{-4}$ s^{-1}
Fr^2	Squared Froude number	$2.5 \cdot 10^{-3}$ (−)
L^*_{dom}	Cross-bank domain size	35 km
H^*_{sb}	Sand bank height	10 m
n	Parameter controlling sand bank profile's shape and width	10 (−)
λ^*	Bed slope correction factor	1.5 (−)
s^*	Slip parameter	0.01 m s^{-1}
A^*_v	Vertical eddy viscosity	0.04 m^2 s^{-1}
g^*	Gravitational acceleration	9.81 m s^{-2}
$\boldsymbol{U}^*_{0,M2}$	Ambient M2 depth-averaged flow amplitude	0.7 m s^{-1}
θ	M2 orientation w.r.t. along-bank direction	30° (clockwise)
β	Ratio of tidal ellipse's semiminor and semimajor axes	0.1 (−)
$U^*_{0,res}$	Maximum along-bank residual depth-averaged flow velocity	0.01 m s^{-1}
$V^*_{0,res}$	Maximum cross-bank residual depth-averaged flow velocity	0 m s^{-1}
N_y	Number of points in the cross-bank direction	100
N_z	Number of points in the vertical direction	51
P	Truncation number of tidal harmonics	2

When scaling the Exner equation, a second timescale is encountered, that is, the morphological scale

$$T^*_{mor} = \frac{L^* H^*_0 (1 - \epsilon_p)}{\alpha^* \left(H^*_0 U^* \sigma^*\right)^{3/2}} \sim 40 \text{ yrs}, \tag{9}$$

which is the timescale at which sand waves evolve, yielding the slow time coordinate τ. Because sand banks evolve in the timescales of centuries to millennia, here we consider the sand bank to be static, and the only bed evolution is driven by sand waves. Therefore, the sand wave profile is assumed to vary on τ only and variations on t are neglected, that is $h = h(\tau)$. Similarly, the variations of the flow and sediment transport on the morphological timescale τ are assumed to be negligible. The difference in timescales between the independent coordinates t and τ effectively allows us to consider a static sand wave profile when solving for hydrodynamics and sediment transport. This is known as the quasi-stationary approach.

The resulting scaled model equations are

$$\frac{\partial u}{\partial t} + u\frac{\partial u}{\partial x} + v\frac{\partial u}{\partial y} + w\frac{\partial u}{\partial z} - fv = -F - \frac{\partial \zeta}{\partial x} + A_v \frac{\partial^2 u}{\partial z^2}, \tag{10a}$$

$$\frac{\partial v}{\partial t}+u\frac{\partial v}{\partial x}+v\frac{\partial v}{\partial y}+w\frac{\partial v}{\partial z}+fu=-G-\frac{\partial \zeta}{\partial y}+A_{\mathrm{v}}\frac{\partial^2 v}{\partial z^2}, \tag{10b}$$

$$\frac{\partial u}{\partial x}+\frac{\partial v}{\partial y}+\frac{\partial w}{\partial z}=0, \tag{10c}$$

$$A_{\mathrm{v}}\frac{\partial u}{\partial z}=A_{\mathrm{v}}\frac{\partial v}{\partial z}=0, w=0 \quad \text{at } z=0, \tag{11}$$

$$A_{\mathrm{v}}\frac{\partial u}{\partial z}=su, \quad A_{\mathrm{v}}\frac{\partial v}{\partial z}=sv, \quad w=u\frac{\partial z}{\partial x}+v\frac{\partial z}{\partial y} \quad \text{at } z=-H+h, \tag{12}$$

$$\frac{\partial h}{\partial \tau}=-\langle \nabla_{\mathrm{h}}\cdot \boldsymbol{q}_{\mathrm{b}}\rangle, \quad \boldsymbol{q}_{\mathrm{b}}=|\boldsymbol{\tau}_{\mathrm{b}}|^{3/2}\left(\frac{\boldsymbol{\tau}_{\mathrm{b}}}{|\boldsymbol{\tau}_{\mathrm{b}}|}-\lambda\nabla_{\mathrm{h}}(-H+h)\right)-\boldsymbol{q}_{\mathrm{b,bank}}, \quad \nabla_{\mathrm{h}}=\left(\frac{\partial}{\partial x},\frac{\partial}{\partial y}\right). \tag{13}$$

Because the squared Froude number turns out to be small $\left(\mathrm{Fr}^2=U^{*2}/(g^*H^*)\ll 1\right)$, we have applied the rigid lid approximation, by which the sea surface boundary conditions are applied at $z=0$ instead of at $z=\zeta$. In Equation 13, $\langle\cdot\rangle=1/T_{\mathrm{M2}}\int_0^{T_{\mathrm{M2}}}\cdot\,\mathrm{d}t$ denotes tidal averaging. We consider only the tidally averaged component of the sediment transport in the Exner Equation 13 because changes in sand wave morphology take place at a much longer timescale (T^*_{mor}) than the tidal period (T^*_{M2}). The above equations are supplemented with periodic boundary conditions in the cross-bank direction.

3.2. Linear Stability Analysis Framework

We study the stability of a sand bank, on top of which a topographic perturbation may grow or decay. To this end, we write the system's state as the sum of a basic state and a perturbed state, according to

$$\phi=\phi_0+\epsilon\phi_1+\text{h.o.t.} \quad \text{with} \quad \phi=\left(\boldsymbol{u},\zeta,\boldsymbol{q}_{\mathrm{b}},h\right)^{\top}, \tag{14}$$

in which we shall ignore higher order terms (h.o.t.) in ϵ. Here, ϵ is a small expansion parameter representing the ratio of sand wave height and ambient water depth, and ϕ represents the properties of the system. The ϕ_0 contribution represents the topography, flow and sediment transport over the sand bank in the absence of sand waves; the ϕ_1 contribution represents the sand wave topography and associated flow, sea surface elevation and sediment transport. In the following subsections, we further detail the specification and calculations of the basic state (Section 3.3) and the numerical method to solve the perturbed state (Section 3.4).

3.3. Basic State

The basic state describes the 3D flow patterns (u,v,w) and the sediment transport arising from them $\left(\boldsymbol{q}_{\mathrm{b}}\right)$, over the imposed sand bank topography,

$$z=z_{\mathrm{b},0}(y)=-H(y). \tag{15}$$

As introduced in Section 2, the sand bank topography is in morphodynamic equilibrium at the morphological timescale of interest. This assumption is equivalent to imposing a zero divergence of sediment transport, requiring

$$\boldsymbol{q}_{\mathrm{b,bank}}=|\boldsymbol{\tau}_{\mathrm{b},0}|^{3/2}\left(\frac{\boldsymbol{\tau}_{\mathrm{b},0}}{|\boldsymbol{\tau}_{\mathrm{b},0}|}+\lambda\nabla_{\mathrm{h}}H\right). \tag{16}$$

Note that at this point, any flow structure may be obtained from choosing the forcings F and G appropriately. Our goal is to force a flow over a sand bank resembling observations. Yet, flow observations in the vicinity of a sand bank are scarce. Therefore, we combine results from observational, idealized and complex modeling studies to specify the imposed depth-averaged flow over the sand bank. The main depth-averaged flow components defining the flow over a sand bank appear to be the semidiurnal and residual components (Caston & Stride, 1970; Huthnance, 1973; Loder, 1980; van den Eynde et al., 2010).

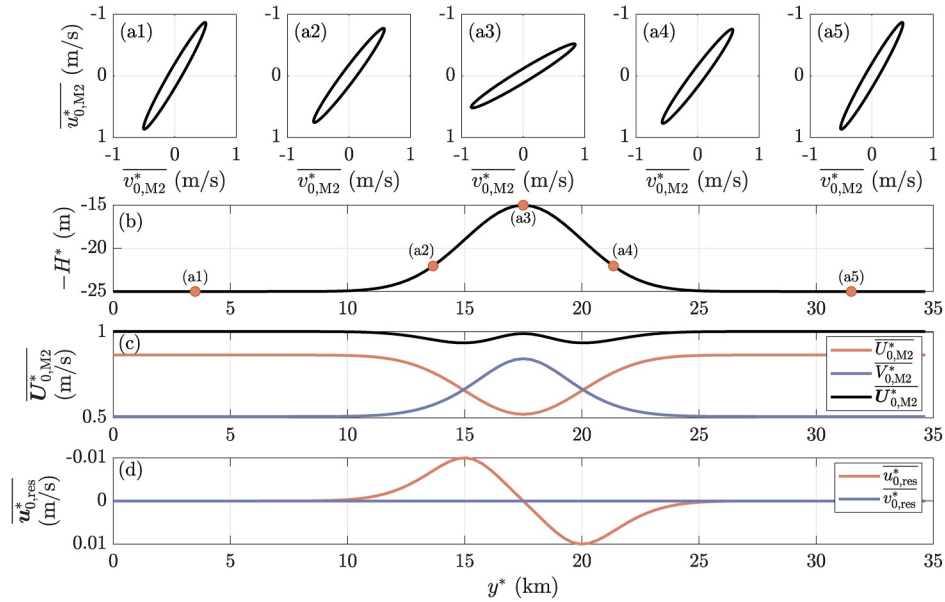

Figure 3. Imposed, unscaled basic state depth-averaged flow over a sand bank. Row (a) shows the tidal ellipses at five locations, highlighted in the topography plot in panel (b). Panel (c) shows the M2 amplitude, and (d) the residual components of the flow. Note that the vertical axes of (a) and (d) have been reversed so that the plot shows a top view of the flow over the sand bank.

Regarding the tidal flow, far from the sand bank we impose an ambient M2 tidal ellipse characterized by a depth-averaged amplitude $\overline{\boldsymbol{U}^*_{0,\mathrm{M2}}}$ (with an overbar denoting depth-averaging), a ratio of tidal ellipse's semiminor and semimajor axes β, and an inclination angle θ with respect to the x direction. We know that the cross-bank M2 flow component, $\overline{V^*_{0,\mathrm{M2}}}$, is mainly controlled by continuity, while the along-bank component, $\overline{U^*_{0,\mathrm{M2}}}$, is mainly controlled by bottom friction (Dyer & Huntley, 1999; Huthnance, 1973; Loder, 1980). Thus, $\overline{V^*_{0,\mathrm{M2}}}$ is inversely proportional to the depth H^* (accelerates on shallower regions), while $\overline{U^*_{0,\mathrm{M2}}}$ is linearly proportional to the depth H^* (decelerates on shallower regions). This results in the typical veering of the ellipse over the bank topography, as shown in Figure 3a.

For the depth-averaged residual along-bank current, we use the expression found by Loder (1980), which is proportional to the local bed slope in the cross-bank direction (Figure 3c). Yet, we scale it in order to obtain residual flow velocities of the order of those observed (i.e., $U^*_{0,\mathrm{res}} \sim 1$ cm/s, Huthnance, 1973) or those obtained by modeling studies (e.g., the study on the Kwinte Bank, Belgium, by van den Eynde et al., 2010). Following the assumptions of Loder (1980) and the fact that observational studies do not report a cross-bank residual flow (Caston & Stride, 1970; Huthnance, 1973), we impose a zero depth-averaged cross-bank residual current, $v^*_{0,\mathrm{res}} = 0$ for all y. Appendix A contains the expression for the depth-averaged residual along-bank current of Loder (1980) rewritten with our notation.

In this study we require the flow associated with overtides (M4, M6, …) to vanish in depth-averaged sense. However, this still allows for a nonzero vertical profile of these components. By default, we resolve the flow up to the M4 tidal component. The method to compute the 3D structure of the imposed depth-averaged flow over the sand bank, that is, $u_0(y,z,t)$, $v_0(y,z,t)$ and $w_0(y,z,t)$ is presented in Appendix B. Particularly, we define a new coordinate system, where the vertical coordinate is scaled in order to have a rectangular domain, and we choose the tidal forcings F and G in order to impose the depth-averaged flow velocities presented in this section.

The resulting near-bed M2 flow behaves qualitatively similar to the imposed depth-averaged flow. The along-bank (cross-bank) component is (inversely) proportional to $H(y)$ (not shown here). The resulting 3D residual flow consists of a near-bed clockwise and uphill residual circulation around the sand bank (Figures 4b–4d), realistic for sand banks in the Northern Hemisphere. Both horizontal components of the residual flow are zero in the region where the cross-bank derivative of the topography is zero (Figure 4a) because the imposed depth-

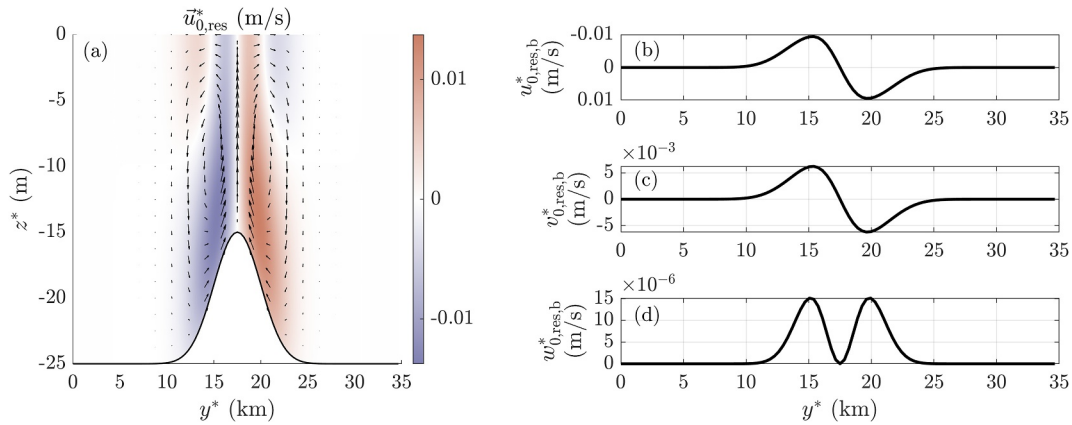

Figure 4. 3D properties of the residual flow in the basic state: (a) along-bank flow in color and the cross-bank and vertical components with arrows. (b–d) Flow components at the seabed. Note that the vertical axis of (b) is reversed in order to show a top view of the along-bank flow on the sand bank.

averaged along-bank residual flow also vanishes in that region (on the sand bank crest and flat part far from the sand bank, Figure 3d).

3.4. Perturbed State

We determine the stability of our basic state by studying the evolution of bed perturbations that are periodic in the along-bank direction (x) and have a yet unknown structure in the cross-bank direction (y):

$$h_1(x,y,\tau) = \hat{h}_1(y,\tau)\exp(ikx) + \text{c.c.}, \tag{17}$$

with c.c. denoting the complex conjugate. Here, k is an arbitrary and prescribed topographic wavenumber (in the along-bank direction, real-valued), and the complex quantity $\hat{h}_1(y,\tau)$ describes the cross-bank topographic structure and temporal behavior, which will follow from the eigenvalue problem presented further below. The components of the perturbed flow, the perturbed sea surface elevation and the perturbed sediment transport have a similar spatial structure, so we may write

$$\begin{aligned} \boldsymbol{u}_1 &= \hat{\boldsymbol{u}}_1(y,z,t)\exp(ikx) + \text{c.c.}, \\ \zeta_1 &= \hat{\zeta}_1(y,t)\exp(ikx) + \text{c.c.}, \\ \boldsymbol{q}_{\mathrm{b},1} &= \hat{\boldsymbol{q}}_{\mathrm{b},1}(y,t)\exp(ikx) + \text{c.c.}. \end{aligned} \tag{18}$$

To find the solution $\boldsymbol{\phi}_1 = (\boldsymbol{u}_1, \zeta_1, \boldsymbol{q}_{\mathrm{b},1}, h_1)^{\mathsf{T}}$, that is the perturbed flow, sea surface elevation, sediment transport, and sand wave topography, we solve the eigenvalue problem posed by the model equations at $\mathcal{O}(\epsilon)$ resulting in eigenmodes for any value of k. The hydrodynamic equations at this order are given by

$$\frac{\partial u_1}{\partial t} + u_0\frac{\partial u_1}{\partial x} + v_0\frac{\partial u_1}{\partial y} + v_1\frac{\partial u_0}{\partial y} + w_0\frac{\partial u_1}{\partial z} + w_1\frac{\partial u_0}{\partial z} - fv_1 = -\frac{\partial \zeta_1}{\partial x} + A_{\mathrm{v}}\frac{\partial^2 u_1}{\partial z^2}, \tag{19a}$$

$$\frac{\partial v_1}{\partial t} + u_0\frac{\partial v_1}{\partial x} + v_0\frac{\partial v_1}{\partial y} + v_1\frac{\partial v_0}{\partial y} + w_0\frac{\partial v_1}{\partial z} + w_1\frac{\partial v_0}{\partial z} + fu_1 = -\frac{\partial \zeta_1}{\partial y} + A_{\mathrm{v}}\frac{\partial^2 v_1}{\partial z^2}, \tag{19b}$$

$$\frac{\partial u_1}{\partial x} + \frac{\partial v_1}{\partial y} + \frac{\partial w_1}{\partial z} = 0, \tag{19c}$$

where the basic state affects the first order solution. Note that the forcing terms F, G do not have a perturbed component. The sea surface boundary conditions read

$$A_v \frac{\partial u_1}{\partial z} = A_v \frac{\partial v_1}{\partial z} = w_1 = 0 \quad \text{at } z = 0. \tag{20}$$

The seabed boundary conditions are expanded around $z = -H(y)$ in order to find an expression evaluated at $z = -H(y)$ instead of $z = -H(y) + \epsilon h_1(x, y, \tau)$. This results at $\mathcal{O}(\epsilon)$ in

$$A_v \left(\frac{\partial u_1}{\partial z} + h_1 \frac{\partial^2 u_0}{\partial z^2} \right) = s \left(u_1 + h_1 \frac{\partial u_0}{\partial z} \right) \quad \text{at } z = -H(y), \tag{21a}$$

$$A_v \left(\frac{\partial v_1}{\partial z} + h_1 \frac{\partial^2 v_0}{\partial z^2} \right) = s \left(v_1 + h_1 \frac{\partial v_0}{\partial z} \right) \quad \text{at } z = -H(y), \tag{21b}$$

$$w_1 + h_1 \frac{\partial w_0}{\partial z} = u_0 \frac{\partial h_1}{\partial x} + v_0 \frac{\partial h_1}{\partial y} - \left(v_1 + h_1 \frac{\partial v_0}{\partial z} \right) \frac{\mathrm{d}H}{\mathrm{d}y} \quad \text{at } z = -H(y). \tag{21c}$$

The bed evolution is governed by the $\mathcal{O}(\epsilon)$-contribution of the Exner equation, which is given by

$$\frac{\partial h_1}{\partial \tau} = -\langle \nabla_h \cdot \boldsymbol{q}_{b,1} \rangle. \tag{22}$$

Analogous to our calculation of the basic state, we transform the vertical coordinate in order to have a rectangular domain. The first order expression for the divergence of sediment transport, $\nabla_h \cdot \boldsymbol{q}_{b,1}$, together with the flow equations in the transformed coordinate system are given in Appendix C.

In order to solve the eigenvalue problem posed by Equations 19–22, we expand the complex quantities depending on t, $\hat{\boldsymbol{u}}_1, \hat{\zeta}_1, \hat{\boldsymbol{q}}_{b,1}$, in Fourier components according to Equation 8. Therefore, the derivatives with respect to t take the form $\partial/\partial t \equiv ip$.

Given the expression for the perturbed sediment transport (see Appendix C), the system of equations (including Exner and flow equations, as well as boundary conditions) is linear in the perturbed physical quantities, yielding

$$\mathcal{L}\phi_1 = \mathcal{M} \frac{\partial \phi_1}{\partial \tau}, \tag{23}$$

where $\mathcal{L}$ and $\mathcal{M}$ are linear operators. Due to the quasi-stationary approach, all elements of the right-hand-side in Equation 23 are zero, except those corresponding to the bed perturbation and corresponding to the Exner equation. Therefore the need for the operator $\mathcal{M}$. Equation 23 allows for solutions of the form

$$\phi_1 = \Phi_1 \exp(\omega \tau), \tag{24}$$

resulting in the Eigenvalue Problem

$$\mathcal{L}\Phi_1 = \mathcal{M}\omega\Phi_1, \quad \text{with } \omega = \omega_r + i\omega_i. \tag{25}$$

Here, Φ_1 is an eigenmode of the system with a corresponding eigenvalue ω.

The discretized version of Equation 25 is

$$\left(\begin{array}{c|c} \mathbf{A} & \mathbf{B} \\ \hline \mathbf{C} & \mathbf{D} \end{array} \right) \begin{pmatrix} \hat{u}_1 \\ \hat{v}_1 \\ \hat{w}_1 \\ \hat{\zeta}_1 \\ \check{h}_1 \end{pmatrix} = \omega \left(\begin{array}{c|c} \mathbf{0} & \mathbf{0} \\ \hline \mathbf{0} & \mathbf{I} \end{array} \right) \begin{pmatrix} \hat{u}_1 \\ \hat{v}_1 \\ \hat{w}_1 \\ \hat{\zeta}_1 \\ \check{h}_1 \end{pmatrix}, \tag{26}$$

where the left-hand-side matrix represents the linear differential operator $\mathcal{L}$, formed by the matrices **A** and **B**, which describe the hydrodynamic equations, including boundary conditions; and the matrices **C** and **D**, which describe the Exner equation. Note that we have omitted the sediment transport in the perturbed solution vector by

substituting the flow velocities into the perturbed Exner Equation 22. Furthermore, because of the quasi-stationary approach, the variations of $\hat{u}_1, \hat{v}_1, \hat{w}_1, \hat{\zeta}_1$ on the morphological timescale τ are assumed to be negligible, yielding the matrix in the right-hand-side (RHS) of Equation 26 to be almost entirely zero. The non-zero elements on the RHS matrix originate from the Exner Equation 22.

Following Equation 26, each eigenmode Φ_1 is characterized by a topography and the corresponding flow and sea surface elevation $\left(\hat{\boldsymbol{u}}_1, \hat{\zeta}_1\right)$. Furthermore, the a priori unknown cross-bank dependency of the topography makes it necessary to discretize the model equations and variables in the cross-bank direction.

The topographic part of the solution to the Eigenvalue Problem can be expressed as

$$h_1(x, y, \tau) = \check{h_1}(y)\exp(ik(x - c_{\mathrm{mig},x}\tau))\exp(\omega_r\tau) + \text{c.c.}, \tag{27}$$

where $\check{h_1}(y)$ is the corresponding y structure of the perturbed topography of an eigenmode of $\mathcal{L}$, ω_r is the associated growth rate, while $c_{\mathrm{mig},x}$ is the mode's migration rate in the along-bank direction, which is related to ω_i as $c_{\mathrm{mig},x} = -\omega_i/k$, k being the topographic wavenumber.

Numerically, we discretize the variables using Finite Differences in space (y, z) and a Fourier expansion for the fast time (t). Therefore, variables have N_y components in y-space, N_z components in z-space, and $2P + 1$ components in Fourier space, with truncation number P as introduced in Section 3.1.

The matrix system in Equation 26 yields N_y generalized eigenvectors, each with its corresponding eigenvalue ω. Note that every value of the topographic wave number k yields a different set of matrices **A**–**D**, each yielding N_y eigenvectors $\check{h_1}(y)$ each describing a different cross-bank structure of the sand wavefield. By default, $P = 2, N_y = 100, N_z = 51$, which make the matrices in Equation 26 to have $\sim 8 \cdot 10^4 \times 8 \cdot 10^4$ elements ($3(2P + 1)N_yN_z$ components for the flow, $(2P + 1)N_y$ components for the sea surface elevation, and N_y components for the bed perturbation). Equation 26 is solved using standard matrix techniques in MATLAB (code available at Portos-Amill et al., 2025).

4. Results

4.1. Fastest Growing Mode

To illustrate how an underlying sand bank topography affects sand wave formation, let us consider the flatbed case (as reference), as well as a range of sand bank topographies with gradually increasing sand bank height, and the respective basic state flow patterns. All cases are forced with the same ambient M2 tidal ellipse, which is locally affected by the sand bank as described in Section 3.3 (except for the flatbed case, for which the depth-averaged flow is uniform in y). In particular, the flow over the 10 m high sand bank is the one presented in Section 3.3.

Figure 5 shows the FGM (the mode with the largest growth rate) for all four cases. The FGM over a flatbed constitutes a sand wavefield with a uniform orientation, $\theta_{sw} \sim 80°$ (Figure 5b1). Here we have defined the orientation of a sand wavefield as the angle of the sand wave crests with respect to the positive y direction, positive angles being anticlockwise.

Strikingly, with the presence of a sand bank, this sand wave pattern only covers the trough region, showing zero amplitudes (white strip in Figure 5b) on the flanks and crest. The region to which the nonzero pattern of the FGM is confined becomes narrower for higher sand banks (from ~15 km to ~8 km at either side of the sand bank crest, Figure 5b2-4), while the sand wave orientation remains roughly the same (from ~80° to ~75°, Figure 5b2-4). The along-bank topographic wavenumber also remains the same, $k_{\mathrm{FGM}} = 0.012\ \mathrm{m}^{-1}$, corresponding to an along-bank wavelength of ~523 m. Note that none of the modes shown in Figure 5 displays migration. This is because of the choice in basic state, in this case with a symmetric ambient current. In Section 4.2 we will see that other modes have different characteristics, such as migration rate and region with a nonzero amplitude.

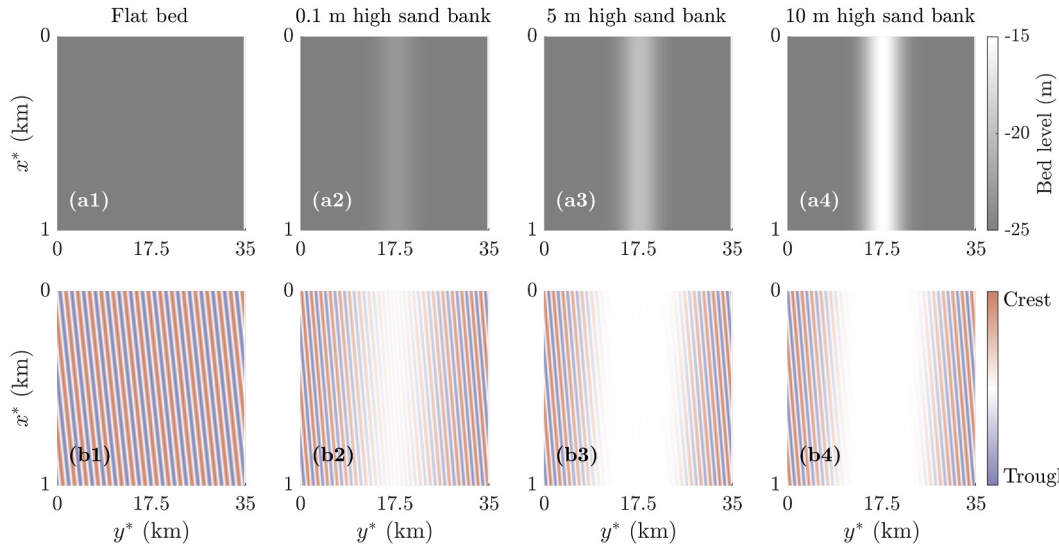

Figure 5. Results of linear stability analysis for different background topographies. The leftmost column (1) shows results for a flatbed, and columns (2–4) show results for gradually increasing sand bank heights ($H^*_{sb} = 0.1, 5, 10$ m, respectively). The top row (a) shows the sand bank topography, and row (b) shows the topography of the FGM. Note the different scales in x^* and y^*, which affect the visual perception of sand wave orientation. The x^* axes are reversed in order to show a top view.

4.2. Variations in Sand Wave Patterns Across the Sand Bank

As shown in Figure 5, as the basic state flow conditions vary over the underlying sand bank, the sand wave pattern of the FGM turns out to be spatially confined, that is, not covering the entire domain. Therefore, we need to consider other modes, with lower growth rates but still positive, in order to characterize the sand waves that grow in the regions where the FGM has (close to) zero amplitude. To analyze this, we define the region of coverage of an eigenmode. We consider an eigenmode to cover an arbitrary region if its amplitude within this region is at least 10% of its maximum amplitude throughout the entire domain (to be discussed in Section 5.1). The eigenmodes that explain sand wave formation in the entire domain including the sand bank are those with the largest growth rates that collectively cover the entire domain. Therefore, each point in y needs to correspond to a nonzero amplitude point of at least one of the modes we consider. Figures 6a–6d shows the eigenmodes with the largest growth rates that explain sand wave formation everywhere across a 10 m high sand bank. Black dots represent the points in y where each mode locally serves as FGM, and thus will dominate over the other modes and determine local sand wave characteristics.

Note that the x^* and y^* axes in panels (a–d) of Figure 6 have different scales, which produces a distorted view of sand wave orientation. In order to better visualize sand wave orientation, Figure 7 once again shows the modes in panels (a1) and (c4) of Figure 6 but now with equal scales on both axes. Black lines denote the cross-bank points where each mode serves as the local FGM.

The local values for sand wave migration and orientation are given by those of the local FGM (Figures 6e and 6f). Our results show that sand wave migration is zero far from the sand bank, whereas it attains nonzero values from $\sim$10 km from the crest of the sand bank, with faster migration closer to the sand bank crest (Figure 6e). Migration rates attain positive (negative) values on the right (left) flank of the sand bank. This coincides with the direction of the near-bed residual current (Figures 4a and 4b) and implies a clockwise migration of sand waves around the sand bank. Note that precisely at the bank crest ($y^* = 17.5$ km) two modes serve as local FGM (with exactly the same growth rates, modes in Figures 6c4 and 6d4). Therefore, the sand wave characteristics at the central point are computed as the average of these two modes, here leading to a zero migration rate.

Sand waves located in the flatbed region away from the sand bank are oriented at an angle of $\theta_{sw} \sim 75°$, and veer toward the crest if they are located halfway between the flatbed regions and the sand bank crest $(\theta_{sw} \sim 45° - 60°)$, close to where the cross-bank derivative of the sand bank topography is maximum (Figures 6f

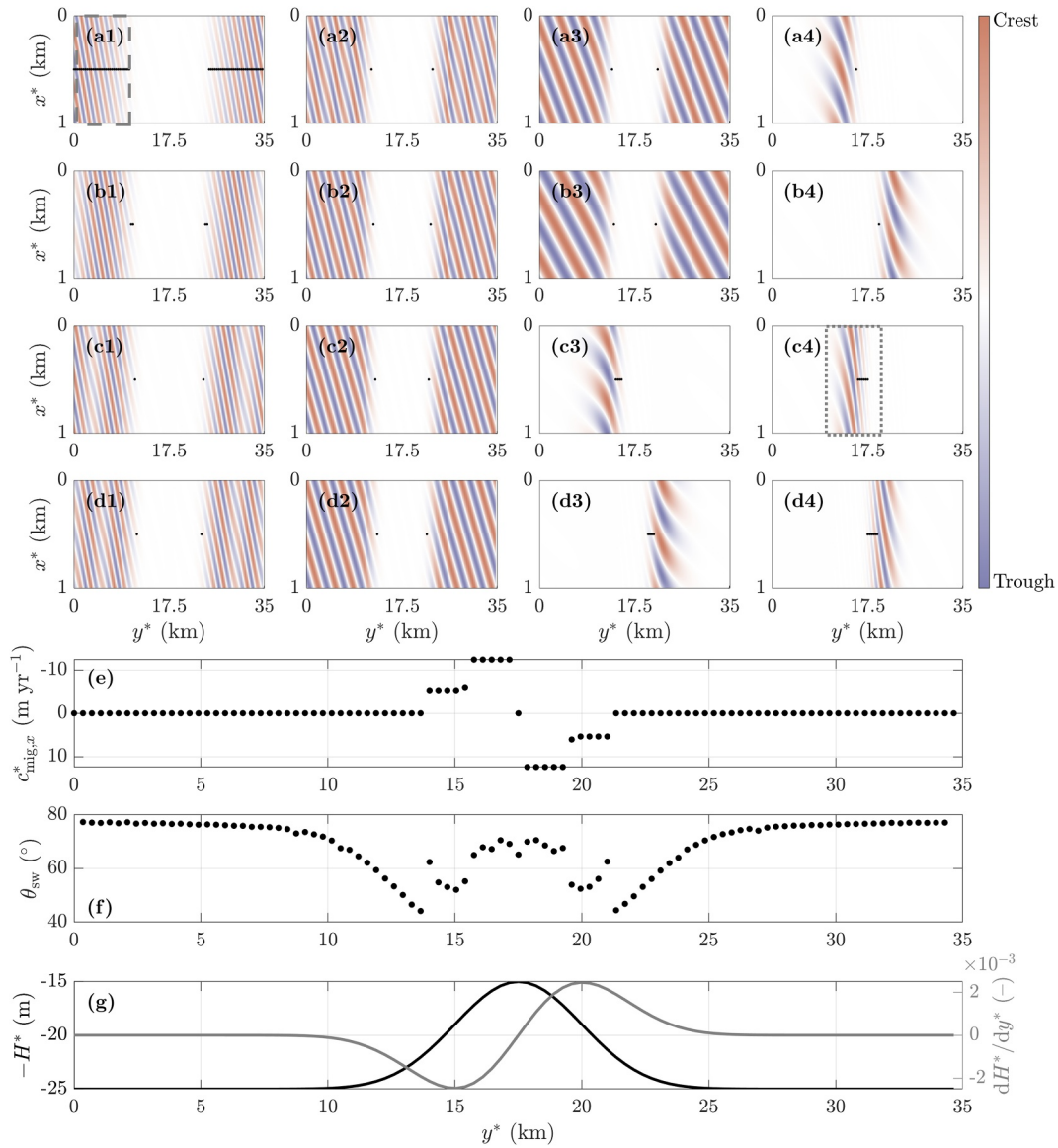

Figure 6. (a–d): Top view of modes with the largest growth rate that explain sand wave characteristics across the entire sand bank. They are ordered in decreasing growth rate from top to bottom and from left to right. Black dots show the cross-bank points where each mode serves as the local FGM. (e) Sand wave migration rate, obtained from the local FGM. (f) Same as (e) but for the sand wave orientation. (g) Sand bank profile $H^*(y^*)$ and its cross-bank derivative. Note that the vertical axes of (a–e) are reversed in order to show top views. Note the different scales in x^* and y^* axes in (a–d), which affect the visual perception of sand wave orientation. Panel (a1) shows the same mode as panel (b4) of Figure 5. Growth and migration rates of the modes in (a–d) are given in Table 2. The dashed and dotted boxes in panels (a1) and (c4) show the regions zoomed-in in Figure 7.

and 6g). The sand waves located on top of the sand bank crest are slightly less oblique than those on the flanks $(\theta_{\mathrm{sw}} \sim 70°)$.

Table 2 summarizes the growth and migration rates of the modes shown in Figures 6a–6d. Note that some modes appear in *pairs*, that is, a set of two modes whose topography is mirrored with respect to the sand bank crest, with identical growth rates and migration rates of identical magnitude yet opposite direction (c3 and d3, a4 and b4, c4 and d4). These specific properties for growth and migration rates are due to the symmetry of the basic state sand bank topography and the corresponding flow over it.

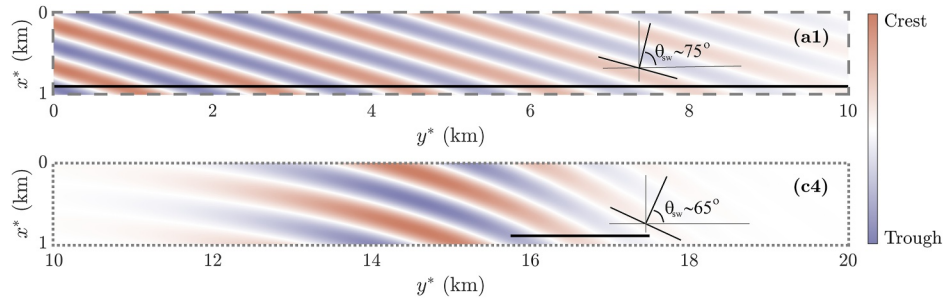

Figure 7. Zoom-in of modes (a1) and (c4) of Figure 6, here plotted using the same scale for the x^* and y^* axes. Analogous to Figure 6, black lines denote the cross-bank points where each mode serves as the local FGM. Each panel includes a visual representation of the local sand wave orientation θ_{sw} as shown in Figure 6f. Note the difference in y^* axis values.

4.3. Other Sand Bank Shapes

The example presented in Sections 4.1 and 4.2, was characterized by a topography and flow patterns that are both symmetric in the cross-bank coordinate. If the symmetry of the basic state sand bank topography and corresponding flow pattern is broken, the resulting modes are no longer symmetric, and thus do not appear in pairs in the strict sense. However, clockwise sand wave migration around the bank still occurs, sand waves growing on the steeper sand bank flank migrate faster than those on the milder flank, while those on the trough far from the sand bank crest do not migrate (see Appendix D for details).

Other simulations with a wider sand bank, and thus a milder slope (not shown here), give modes spreading over a wider region and with lower migration rates. This was already seen in Figure 5 for different sand bank heights. The behavior is qualitatively the same when keeping a constant sand bank height and gradually increasing the width of the sand bank.

Table 2
Growth (ω_r), Along-Bank Migration Rates ($c_{mig,x}$) and Location of Mode on the Sand Bank Corresponding to the Modes Shown in Figure 6

			Part of the sand bank covered by sand waves[a]	
Panel(s) in Figure 6	ω_r (yr^{-1})	$c_{mig,x}$ (m yr^{-1})	Trough	Flanks/Crest
Figure 6a1	1.05	0	✓	✗
Figure 6b1	1.05	0	✓	✗
Figure 6c1	1.05	0	✓	✗
Figure 6d1	1.04	0	✓	✗
Figure 6a2	1.04	0	✓	✗
Figure 6b2	1.03	0	✓	✗
Figure 6c2	1.02	0	✓	✗
Figure 6d2	1.00	0	✓	✗
Figure 6a3	0.97	0	✓	✗
Figure 6b3	0.94	0	✓	✗
Figures 6c3 and 6d3	0.90	∓5.4	✗	✓
Figures 6a4 and 6b4	0.89	∓6.0	✗	✓
Figures 6c4 and 6d4	0.88	∓12.4	✗	✓

Note. Top part summarizes the modes that do not migrate and do not appear in pairs, while the rows on the lower part correspond to migrating pairs of modes. Modes are ordered by decreasing growth rate. [a]The distinction between sand bank trough and flank/crest is somewhat arbitrary. Here, we define trough modes as those that do not migrate and do not appear in pairs for the default symmetric sand bank.

5. Discussion

5.1. Concept of FGM

The results of a linear stability analysis showing sand wave formation over a non-horizontal background topography and associated flow patterns cannot be summarized with the FGM *only*. This is because, unlike the flatbed case, the obtained modes do not generally provide information on sand wave growth across the entire sand bank domain (Figure 5). Linear stability analysis studies generally consider the FGM to be the one describing the sand wave properties because it is the one that would ultimately dominate in the linear regime, despite the existence of other growing modes (e.g., Dodd et al., 2003; Hulscher, 1996). However, in the presence of a non-horizontal background topography, this concept needs to be extended to account for the local coverage of sand wave patterns. Therefore, one needs to consider the growing modes that constitute the set of *local* FGMs for the entire cross-bank domain, such that each considered mode locally serves as FGM of at least one point in y. Note that the nonzero pattern of each mode always extends over an interval in the cross-bank direction.

In Section 4.2, we have defined a coverage threshold of 10% of the maximum amplitude of the perturbation within the domain. If the local amplitude of the eigenmode satisfies this condition, then that eigenmode is considered to provide information of local sand waves. Changing the coverage condition does not qualitatively affect the results of this study. It merely changes the number of modes needed to describe sand wave characteristics, and thus also the quantities computed from them (e.g., migration rate and orientation, Figure 6). Specifically, varying the coverage threshold between 5% and 15% only affects the obtained modes by adding one, and the properties of the sand

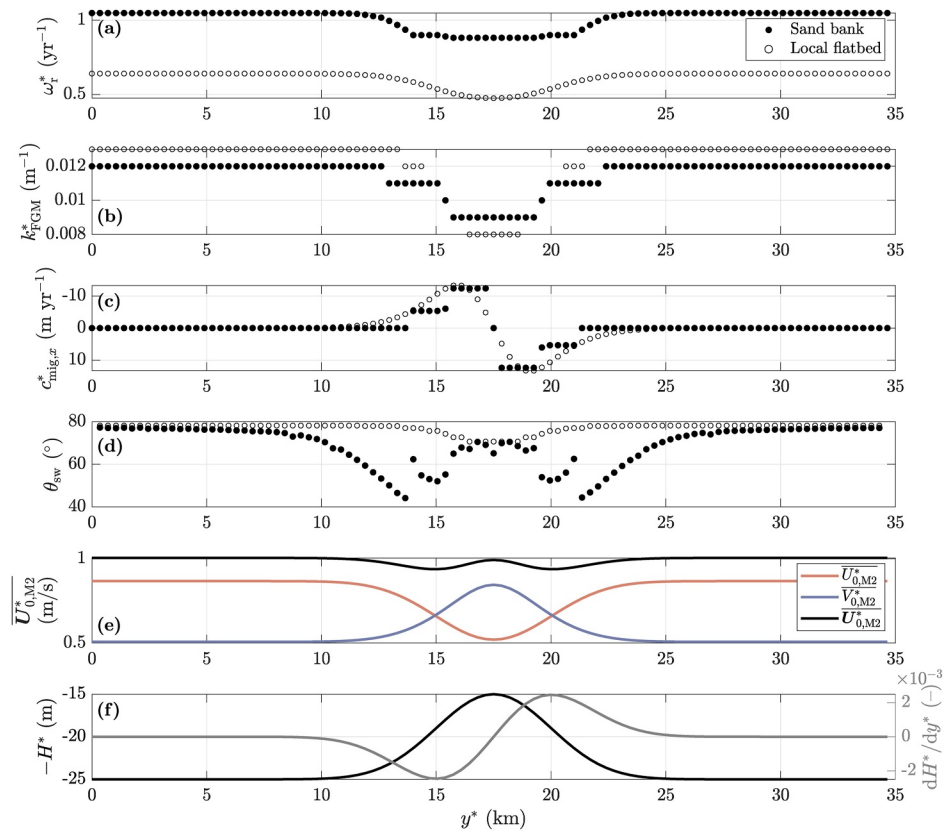

Figure 8. Local sand wave conditions throughout the sand bank compared to a local flatbed model: (f) shows the sand bank topography and cross-bank derivative. Panel (e) shows the imposed depth-averaged flow (already shown in Figure 3c and repeated here for clarity). Panels (a–d) show the local sand wave orientation, migration rate, wave number in along-bank direction and growth rate, respectively. Values obtained with our model are black, and those obtained with a flatbed model with matching local conditions are white. Black dots in panels (c) and (d) show the same results as Figures 6e and 6f, respectively.

wavefield remain qualitatively unchanged. Importantly, the coverage threshold does not affect model results, but it is a post-processing choice.

5.2. Comparison With Local Flatbed Case

Sand wave studies using a linear stability analysis often consider a horizontal background topography, which is not always a realistic representation of nature.

To illustrate the importance of considering the background topography together with a correspondingly spatially varying basic state flow, we compare our model results to those obtained with a flatbed model with the same local conditions. To perform the latter, we run one flatbed model simulation per cross-bank point, each with the local depth and depth-averaged flow (M0 and M2) corresponding to the sand bank basic state at that same point in y (Figure 8). Thus, the main difference between both cases is the presence of the entire sand bank topography, with associated topography and flow gradients.

The growth rate is underestimated across the sand bank domain with the flatbed model, while the along-bank wave number k^*_{FGM} is usually overestimated (Figure 8b). The migration rate is qualitatively similar to that obtained with our model (Figure 8c). Both models compute the same sand wave orientation in the deepest regions and on the sand bank crest (Figure 8d). However, our model yields more oblique sand waves on the flanks of the sand bank, where the cross-bank derivative of the sand bank topography is strongest.

These results show that imposing local flow conditions (taken from some location across the sand bank) in a flatbed model of sand wave formation does not adequately and fully reproduce the physics of sand wave formation on sand banks.

5.3. Comparison With Observations

In this subsection, we compare the model results with observations of sand waves on sand banks. Note that a linear stability analysis assumes nonlinear interactions of the perturbed modes to be negligible. Furthermore, the geometry and processes included in the model are idealized, which is commonly applied in linear stability analysis studies (e.g., Dodd et al., 2003; Hulscher, 1996). Therefore, the goal of this comparison is not to find a quantitative agreement, but to study whether the main characteristics of sand waves on a sand bank are reproduced by our model (qualitatively and within a realistic range of values).

The observations by Caston and Stride (1970), Caston (1972), and Zhou et al. (2022) show a clockwise and slightly uphill sand wave migration around the sand bank in the Northern Hemisphere, as well as a gradual deflection of sand waves as they reach the sand bank crest. Here, we have successfully reproduced the clockwise migration of sand waves, with a locally varying magnitude of the migration rate. This clockwise migration is caused by the clockwise residual current also observed (and imposed in our model) around the sand bank. By definition, our model yields a numerical value for the along-bank migration rate $c_{\mathrm{mig},x}$, which yields an uphill sand wave migration when considered together with the veering of modes toward the sand bank crest.

The obtained magnitudes for the along-bank migration rate (Table 2, Figure 6e) agree qualitatively and in order of magnitude with the observations of, for example, van Landeghem et al. (2012) in the Irish Sea. They found a fairly uniform migration of sand waves at an average of 6 m yr^{-1}, with amplified migration rates in the vicinity of sand banks, where they can reach up to 30 m yr^{-1}. Similarly, Ma et al. (2018) observed sand waves on the steepest flanks of sand ridges to migrate at up to $19 - 33$ m yr^{-1}, while those on milder slopes migrate at rates of $2 - 7$ m yr^{-1}.

Qualitatively, our model is able to reproduce the observed veering of sand waves toward the sand bank crest. Quantitatively, this is more difficult to compare because observations tend not to be as detailed. We obtain sand waves that become more oblique as they get closer to the sand bank flanks. However, once they get close enough to the sand bank crest, they become less oblique again (θ_{sw} slightly increases). The transition from far from the sand bank to the flanks (decreasing θ_{sw}) agrees with the gradual veering toward the crest observed by Caston and Stride (1970) and Caston (1972). The decrease in sand wave obliqueness obtained on the 5 km around the sand bank crestline ($15 < y^* < 20$ km) is not reported in the literature. Future observational studies could focus on sand wave characteristics in the vicinity of the sand bank crest in order to satisfactorily compare these with our model results.

Sand banks are usually asymmetric in nature. Yet, we have focused our efforts on a symmetric sand bank, while adding one asymmetric example in Appendix D. The goal of the present work is to show that a linear stability analysis can be performed on a non-flat seabed, and how the results of the analysis change with respect to the flatbed case, therefore we have used an idealized symmetric sand bank. An in-depth study on the effects of more realistic sand bank shapes and corresponding flow structures on the obtained sand waves is beyond the scope of this work and is left for future research.

5.4. Sensitivity Analysis

We performed a sensitivity analysis for the model parameters (eddy viscosity A_{v}^*, slip parameter s^* and bed slope correction factor λ^*) as well as the parameters controlling the basic flow (ambient M2 depth-averaged flow amplitude $\boldsymbol{U}_{0,\mathrm{M2}}^*$, and maximum along-bank residual depth-averaged flow velocity $U_{0,\mathrm{res}}^*$). Because of space considerations, here we only briefly explain the dependencies obtained (without plots), linking them to the physics of the system and previous studies. Variations of model results yield variations of (some of) the obtained sand wave properties across the sand bank, but the obtained cross-bank dependency of these properties is always maintained, confirming the robustness of our model.

Sand wave formation originates from the balance between the enhancing mechanism regulated by the bed shear stress (first term in the RHS of Equation 5), and the hindering mechanism driven by slope effects (second term in

the RHS of Equation 5). Variations in the model parameters or flow conditions may modify one of these two mechanisms or both of them (Hulscher, 1996).

Regarding the model parameters, an increase in eddy viscosity, results in an increased vertical friction that slows down the flow. This results in weaker flows at the seabed, and, therefore, weaker bed shear stress in this case. This yields a weaker enhancing mechanism and therefore longer sand waves with lower growth rates. The increase in friction also results in lower near-bed residual currents and therefore, lower migration rates. An increase in slip parameter, results in a decrease in slip at the seabed, thus yielding an increase in bed shear stress. This results in an increased enhancing mechanism and, therefore, yields shorter sand waves with higher growth rates. The decreased slip at the seabed also results in increased migration rates. The behavior obtained here was already obtained in earlier flatbed studies (e.g., Besio et al., 2008; Hulscher, 1996). This confirms that the inclusion of a non-uniform background topography does not alter the physics governing the system. An increase in the bed slope correction factor enhances, by definition, slope effects, yielding longer sand waves with lower growth rates, which is physically realistic.

Regarding the forced depth-averaged basic flow, an increase in the ambient M2 depth-averaged flow amplitude results in higher growth rates because of a speed-up of the morphodynamics of the system. Furthermore, it yields increased migration rates because of a stronger residual flow at the seabed, arising from tide-topography interactions. The wavenumber decreases, yielding longer sand waves. The latter result is somewhat counter-intuitive and cannot be directly derived from either the enhancing or the hindering mechanisms. Yet, Borsje et al. (2014) also found this behavior with their flatbed sand wave model. An increased maximum along-bank residual depth-averaged flow velocity mainly affects the migration rate, yielding faster migrating sand waves. This is in agreement with the physics of the system and with previous flatbed studies (e.g., Besio et al., 2008).

6. Conclusion

The aim of this work was to understand how sand wave characteristics (such as shape, migration) are affected by an underlying sand bank topography. To this end, we have developed and analyzed a new model allowing for a linear stability study of a non-horizontal seabed, namely a sand bank on top of which sand waves may grow.

The consideration of a non-uniform basic state yields spatially confined modes as a result of the linear stability analysis. Therefore, the preferred sand wave topographies that tend to form on the sand bank can no longer be *exclusively* described by the fastest growing mode (FGM). Instead, a combination of *local* FGMs that give information about the sand wave characteristics across the entire sand bank should be considered. The resulting sand wavefield has non-uniform cross-bank characteristics (e.g., growth and migration rates, orientation). This adds a new perspective to linear stability analysis studies, where in general *only* the FGM was considered to describe sand wave characteristics.

The sand bank presence and the corresponding residual circulation around the sand bank, yield near-bed uphill and clockwise residual velocities. These result in spatially confined sand wave modes that migrate in an anti-cyclonic sense when located on the flanks of the sand bank ($c_{\mathrm{mig},x} \sim 5$–$12$ m yr^{-1}, for the parameter values chosen here). The sand wave patterns on the flatbed far from the sand bank do not migrate, because the chosen residual currents vanish in these regions. Sand waves located far from the sand bank crest show a relatively uniform orientation of $\theta_{\mathrm{sw}} \sim 75°$, while those on the sand bank flanks veer toward the sand bank crest, with an angle of $\theta_{\mathrm{sw}} \sim 45°$–$60°$. Sand waves on the sand bank crest appear to be less oblique than those neighboring them $\left(\theta_{\mathrm{sw}} \sim 70°\right)$. Observations of sand wave migration rate and shape resemble those modeled.

Finally, comparing our results with those obtained with a flatbed model forced with the same local conditions (depth-averaged flow and depth) shows qualitative and quantitative differences. This demonstrates the important role of background sand bank topography and associated flow patterns on sand wave formation.

Appendix A: Depth-Averaged Residual Along-Bank Current Presented in Loder (1980)

Our expression for the along-bank residual depth-averaged flow velocity is based on that presented in Equation (25) in Loder (1980), which for our reference system and notation reads

$$\overline{u^*_{0,\mathrm{res}}} = \frac{H^*_0 \overline{V^*_{\mathrm{M2,a}}}^2 \frac{\mathrm{d}H^*}{\mathrm{d}y^*}}{2\sigma^{*2}H^{*2}\left(E^{*2}+1\right)^2}\Big(2\sigma^*\left(1-E^{*2}+2E^*E^*_{\mathrm{a}}\right)\frac{1}{\tan\theta}\sin\phi_{\mathrm{R}} + 2\sigma^*\left(E^*\left(2+E^*E^*_{\mathrm{a}}\right)-E^*_{\mathrm{a}}\right)\frac{1}{\tan\theta}\cos\phi_{\mathrm{R}} + f^*E^{*2}\left(2-\frac{H^*_0}{H^*}\right)+f^*\left(3\frac{H^*_0}{H^*}-2\right)\Big). \tag{A1}$$

Here, $\overline{V^*_{\mathrm{M2,a}}}$ is the ambient amplitude of the M2 cross-bank flow, $E^* = \frac{C^*_{\mathrm{D}}\overline{v^*_{0,\mathrm{M2}}}}{\sigma^* H^*}$ with $C^*_{\mathrm{D}} = 2.5\cdot 10^{-3}$ a drag coefficient, E^*_{a} is the ambient value of E^*, and $\phi_{\mathrm{R}} = 6.5°$ is the phase lag between the along-bank and cross-bank ambient M2 flow components (obtained from the imposed M2 flow components presented in Section 3.3).

Appendix B: Basic State: Equations and Solution Method

B1. Equations

The scaled equations governing the flow in the basic state read

$$\frac{\partial u_0}{\partial t} + v_0\frac{\partial u_0}{\partial y} + w_0\frac{\partial u_0}{\partial z} - fv_0 = -F + A_{\mathrm{v}}\frac{\partial^2 u_0}{\partial z^2}, \tag{B1a}$$

$$\frac{\partial v_0}{\partial t} + v_0\frac{\partial v_0}{\partial y} + w_0\frac{\partial v_0}{\partial z} + fu_0 = -G + A_{\mathrm{v}}\frac{\partial^2 v_0}{\partial z^2}, \tag{B1b}$$

$$\frac{\partial v_0}{\partial y} + \frac{\partial w_0}{\partial z} = 0. \tag{B1c}$$

Here, we have applied the scaling procedure presented in Section 3.1 and assumed no variations in the along-bank coordinate x. Note that the terms $-\partial\zeta/\partial y$, $-\partial\zeta/\partial x$ are absent in Equation B1, because these are the pressure gradients associated with the perturbed state; here we have $\zeta_0(x,y,t) = 0$. The subscript $_0$ denotes the basic state.

The boundary conditions at the sea surface and at the seabed read, respectively,

$$\frac{\partial u_0}{\partial z} = \frac{\partial v_0}{\partial z} = 0, w_0 = 0 \quad \text{at } z = 0, \tag{B2}$$

$$A_{\mathrm{v}}\frac{\partial u_0}{\partial z} = su_0,\ A_{\mathrm{v}}\frac{\partial v_0}{\partial z} = sv_0, w_0 = -v_0\frac{\mathrm{d}H}{\mathrm{d}y} \quad \text{at } z = -H(y). \tag{B3}$$

Furthermore, we impose the desired depth-averaged flow for each tidal component p,

$$\overline{u_{0,p}}(y) = \frac{1}{H(y)}\int_{-H(y)}^{0} u_{0,p}\ \mathrm{d}z, \overline{v_{0,p}}(y) = \frac{1}{H(y)}\int_{-H(y)}^{0} v_{0,p}\ \mathrm{d}z. \tag{B4}$$

By default, we set the M0 and M2 depth-averaged flows as described in Section 3.3, and higher harmonics to have a zero depth-averaged value.

B2. Solution Method

We transform to a new coordinate system, scaling the vertical coordinate with the local depth (known as sigma coordinate) and a scaling of the cross-bank coordinate with a small parameter γ reflecting the width of the sand bank topography,

$$\tilde{x} = x,\ \tilde{y} = \gamma y,\ \tilde{z} = \frac{z}{H(\tilde{y})}, \tag{B5}$$

yielding the following derivative operators

$$\frac{\partial}{\partial x} = \frac{\partial}{\partial \tilde{x}},\ \frac{\partial}{\partial y} = \gamma \frac{\partial}{\partial \tilde{y}} - \gamma \tilde{z} \frac{H'}{H} \frac{\partial}{\partial \tilde{z}},\ \frac{\partial}{\partial z} = \frac{1}{H} \frac{\partial}{\partial \tilde{z}}, \tag{B6}$$

where $H' \equiv \mathrm{d}H/\mathrm{d}\tilde{y}$.

The aim of this coordinate transformation is (a) to make the model domain rectangular in order to make the numerical discretisations more straightforward, and (b) to be able to linearize the equations with respect to the small parameter γ, such that

$$\phi_0 = \phi_{0,0} + \gamma\phi_{0,1} + \gamma^2\phi_{0,2} + \ldots, \quad \text{with } \phi_0 = \left(\boldsymbol{u}_0, \zeta_0, \boldsymbol{q}_{\mathrm{b},0}\right). \tag{B7}$$

Note that $\zeta_0 \equiv 0$. Here, we add a second subscript to denote the order in γ. Thus, the expansion $\sum_m \gamma^m \phi_{0,m}$ should converge. Given that we write $H(\tilde{y}) = H(\gamma y)$, the value of γ depends on the domain length as $\gamma = 2\pi/L_{\mathrm{dom}} = 2\pi L^*/L^*_{\mathrm{dom}}$. Furthermore, the local steepness also defines if a solution converges or not, that is, how wide and tall the bank is. The choice of $L^*_{\mathrm{dom}} = 35$ km, $L^* = 5$ km, $H^*_{\mathrm{sb}} = 10$ m and $n = 10$ yields a converging expansion.

Applying the change of coordinates in Equation B5 to the basic state flow equations in B1–B4 and collecting terms of equal order in γ yields

$$\frac{\partial u_{0,m}}{\partial t} + \left[v_0 \frac{\partial u_0}{\partial \tilde{y}}\right]_{m-1} - \tilde{z}\frac{H'}{H}\left[v_0 \frac{\partial u_0}{\partial \tilde{z}}\right]_{m-1} + \frac{1}{H}\left[w_0 \frac{\partial u_0}{\partial \tilde{z}}\right]_m - f v_{0,m} = -F_m + \frac{A_{\mathrm{v}}}{H^2}\frac{\partial^2 u_{0,m}}{\partial \tilde{z}^2}, \tag{B8a}$$

$$\frac{\partial v_{0,m}}{\partial t} + \left[v_0 \frac{\partial v_0}{\partial \tilde{y}}\right]_{m-1} - \tilde{z}\frac{H'}{H}\left[v_0 \frac{\partial v_0}{\partial \tilde{z}}\right]_{m-1} + \frac{1}{H}\left[w_0 \frac{\partial v_0}{\partial \tilde{z}}\right]_m + f u_{0,m} = -G_m + \frac{A_{\mathrm{v}}}{H^2}\frac{\partial^2 v_{0,m}}{\partial \tilde{z}^2}, \tag{B8b}$$

$$\frac{\partial v_{0,m-1}}{\partial \tilde{y}} - \tilde{z}\frac{H'}{H}\frac{\partial v_{0,m-1}}{\partial \tilde{z}} + \frac{1}{H}\frac{\partial w_{0,m}}{\partial \tilde{z}} = 0. \tag{B8c}$$

Here, m denotes the order in γ. Note that for $m = 0$, the bracketed terms related to the order $m - 1$ do not exist and should be treated as zero, this yields $w_{00} = 0$. Note that the forcing terms (F, G) in Equation B2 are also expanded in powers of γ as in Equation B7. Boundary conditions read

$$\frac{\partial u_{0m}}{\partial \tilde{z}} = \frac{\partial v_{0m}}{\partial \tilde{z}} = 0, w_{0m} = 0 \quad \text{at } \tilde{z} = 0, \tag{B9}$$

$$\frac{A_{\mathrm{v}}}{H}\frac{\partial u_{0m}}{\partial \tilde{z}} = s u_{0m},\ \frac{A_{\mathrm{v}}}{H}\frac{\partial v_{0m}}{\partial \tilde{z}} = s v_{0m},\ w_{0m} = -v_{0(m-1)}H' \quad \text{at } \tilde{z} = -1. \tag{B10}$$

The depth-averaged imposed flow reads

$$\overline{u_{0m,p}} = \int_{-1}^{0} u_{0m,p}\ \mathrm{d}\tilde{z},\ \overline{v_{0m,p}} = \int_{-1}^{0} v_{0m,p}\ \mathrm{d}\tilde{z}, \tag{B11}$$

where $\overline{u_{0m,p}}, \overline{v_{0m,p}} = 0$ for all p for $m > 0$. Hence, the desired depth-averaged flow is imposed at order $m = 0$, and higher order contributions only modify the 3D structure of the flow, without altering its depth-averaged structure. This procedure implicitly defines the forms of the forcing terms F_m, G_m, such that the desired depth-averaged flow patterns are achieved.

Note that, from Equation B8c, w_m only depends on $v_{0,m-1}$ for any $m > 0$. For this problem to be well-posed, the vertical integral of $v_{0,m-1}$ needs to be independent of $\tilde{y}$. This is guaranteed by the conditions imposed on the depth-averaged v_0 presented in Section 3.3. Therefore, the basic state problem is well-posed and a solution always exists with the given equations and boundary condition for all m.

The $\mathcal{O}(\gamma^0)$ solution is computed analytically, higher orders in γ are computed semi-analytically. We solve the truncated Fourier components ($P = 2$) using the Fourth Order Runge-Kutta method in a shooting procedure. Integrals in the vertical direction are computed using the Trapezoidal rule, while derivatives in the horizontal direction are computed using a Central Differences scheme. The basic state is solved using 100 points in the y direction and 10^4 points in the z direction. A convergence analysis (not shown here) shows that further increasing the number of points in the y directions does not decrease the error. Finally, the resulting flow components and their derivatives are coarsened to $N_z = 50$ points in the z direction, in order to use it as a forcing to the perturbed state.

Appendix C: Scaled Perturbed State Equations

We define the change of coordinates

$$\tilde{x} = x,\ \ \tilde{y} = y,\ \ \tilde{z} = \frac{z}{H(\gamma y)}. \tag{C1}$$

Note that the $\tilde{y}$ coordinate transformation is not the same as in the Basic State (Equation B5). Now, γ is treated as an ordinary parameter of the equations, no longer as an expansion parameter.

The scaled equations governing the perturbed flow read

$$\begin{aligned}\frac{\partial \hat{u}_1}{\partial t} + iku_0\hat{u}_1 + v_0\frac{\partial \hat{u}_1}{\partial \tilde{y}} - \frac{v_0\tilde{z}}{H}\frac{\mathrm{d}H}{\mathrm{d}\tilde{y}}\frac{\partial \hat{u}_1}{\partial \tilde{z}} + \hat{v}_1\frac{\partial u_0}{\partial \tilde{y}} - \frac{\hat{v}_1\tilde{z}}{H}\frac{\mathrm{d}H}{\mathrm{d}\tilde{y}}\frac{\partial u_0}{\partial \tilde{z}} + \\ + \frac{w_0}{H}\frac{\partial \hat{u}_1}{\partial \tilde{z}} + \frac{\hat{w}_1}{H}\frac{\partial u_0}{\partial \tilde{z}} - f\hat{v}_1 = -\frac{\partial \hat{\zeta}_1}{\partial \tilde{x}} + \frac{A_v}{H^2}\frac{\partial^2 \hat{u}_1}{\partial \tilde{z}^2},\end{aligned} \tag{C2a}$$

$$\begin{aligned}\frac{\partial \hat{v}_1}{\partial t} + iku_0\hat{v}_1 + v_0\frac{\partial \hat{v}_1}{\partial \tilde{y}} - \frac{v_0\tilde{z}}{H}\frac{\mathrm{d}H}{\mathrm{d}\tilde{y}}\frac{\partial \hat{v}_1}{\partial \tilde{z}} + \hat{v}_1\frac{\partial v_0}{\partial \tilde{y}} - \frac{\hat{v}_1\tilde{z}}{H}\frac{\mathrm{d}H}{\mathrm{d}\tilde{y}}\frac{\partial v_0}{\partial \tilde{z}} + \\ + \frac{w_0}{H}\frac{\partial \hat{v}_1}{\partial \tilde{z}} + \frac{\hat{w}_1}{H}\frac{\partial v_0}{\partial \tilde{z}} + f\hat{u}_1 = -\frac{\partial \hat{\zeta}_1}{\partial \tilde{y}} + \frac{A_v}{H^2}\frac{\partial^2 \hat{v}_1}{\partial \tilde{z}^2},\end{aligned} \tag{C2b}$$

$$\frac{\partial \hat{u}_1}{\partial \tilde{x}} + \frac{\partial \hat{v}_1}{\partial \tilde{y}} - \frac{\tilde{z}}{H}\frac{\mathrm{d}H}{\mathrm{d}\tilde{y}}\frac{\partial \hat{v}_1}{\partial \tilde{z}} + \frac{1}{H}\frac{\partial \hat{w}_1}{\partial \tilde{z}} = 0, \tag{C2c}$$

supplemented with the following the boundary conditions:

$$\frac{\partial \hat{u}_1}{\partial \tilde{z}} = \frac{\partial \hat{v}_1}{\partial \tilde{z}} = \hat{w}_1 = 0 \quad \text{at } \tilde{z} = 0, \tag{C3}$$

$$A_v\left(\frac{1}{H}\frac{\partial \hat{u}_1}{\partial \tilde{z}} + \frac{\check{h}_1}{H^2}\frac{\partial^2 u_0}{\partial \tilde{z}^2}\right) = s\left(\hat{u}_1 + \frac{\check{h}_1}{H}\frac{\partial u_0}{\partial \tilde{z}}\right) \quad \text{at } \tilde{z} = -1, \tag{C4a}$$

$$A_v\left(\frac{1}{H}\frac{\partial \hat{v}_1}{\partial \tilde{z}} + \frac{\check{h}_1}{H^2}\frac{\partial^2 v_0}{\partial \tilde{z}^2}\right) = s\left(\hat{v}_1 + \frac{\check{h}_1}{H}\frac{\partial v_0}{\partial \tilde{z}}\right) \quad \text{at } \tilde{z} = -1, \tag{C4b}$$

$$\hat{w}_1 + \frac{\check{h}_1}{H}\frac{\partial w_0}{\partial \tilde{z}} = u_0\frac{\partial \check{h}_1}{\partial \tilde{x}} + v_0\frac{\partial \check{h}_1}{\partial \tilde{y}} - \frac{\mathrm{d}H}{\mathrm{d}\tilde{y}}\left(\hat{v}_1 + \frac{\check{h}_1}{H}\frac{\partial v_0}{\partial \tilde{z}}\right) \quad \text{at } \tilde{z} = -1. \tag{C4c}$$

The components of the divergence of the scaled sediment transport read

$$\begin{aligned}\frac{\partial \hat{q}_{\mathrm{b},1,x}}{\partial \tilde{x}} = s^{3/2}\Bigg(&\left(\left(u_0^2+v_0^2\right)^{1/4} + \frac{1}{2}\left(u_0^2+v_0^2\right)^{-3/4}u_0^2\right)ik\hat{u}_1 + \\ &\frac{1}{2}\left(u_0^2+v_0^2\right)^{-3/4}v_0u_0ik\hat{v}_1 + \\ &\Bigg(\left(u_0^2+v_0^2\right)^{1/4}\frac{1}{H}\frac{\partial u_0}{\partial \tilde{z}} + \frac{u_0}{2}\left(u_0^2+v_0^2\right)^{-3/4}\left(\frac{u_0}{H}\frac{\partial u_0}{\partial \tilde{z}} + \frac{v_0}{H}\frac{\partial v_0}{\partial \tilde{z}}\right) - \\ &\lambda\left(u_0^2+v_0^2\right)^{3/4}ik\Bigg)ik\check{h}_1\Bigg) \quad \text{at } \tilde{z} = -1\end{aligned} \tag{C5a}$$

$$\begin{aligned}\frac{\partial \hat{q}_{\mathrm{b},1,y}}{\partial \tilde{y}} = s^{3/2}\Bigg(&\left(\hat{u}_1\frac{\partial}{\partial \tilde{y}} + \frac{\partial \hat{u}_1}{\partial \tilde{y}}\right)\left(\frac{1}{2}\left(u_0^2+v_0^2\right)^{-3/4}u_0v_0 + \frac{3}{2}\lambda\frac{\mathrm{d}H}{\mathrm{d}\tilde{y}}\left(u_0^2+v_0^2\right)^{-1/4}u_0\right) + \\ &\left(\hat{v}_1\frac{\partial}{\partial \tilde{y}} + \frac{\partial \hat{v}_1}{\partial \tilde{y}}\right)\left(\left(u_0^2+v_0^2\right)^{1/4} + \frac{1}{2}\left(u_0^2+v_0^2\right)^{-3/4}v_0^2 + \frac{3}{2}\lambda\frac{\mathrm{d}H}{\mathrm{d}\tilde{y}}\left(u_0^2+v_0^2\right)^{-1/4}v_0\right) + \\ &\left(\check{h}_1\frac{\partial}{\partial \tilde{y}} - \frac{\partial \check{h}_1}{\partial \tilde{y}}\lambda\frac{\partial}{\partial \tilde{y}}\left(\left(u_0^2+v_0^2\right)^{3/4}\right)\right)\Bigg(\left(u_0^2+v_0^2\right)^{1/4}\frac{1}{H}\frac{\partial v_0}{\partial \tilde{z}} + \\ &\frac{1}{2}\left(u_0^2+v_0^2\right)^{-3/4}v_0\left(\frac{u_0}{H}\frac{\partial u_0}{\partial \tilde{z}} + \frac{v_0}{H}\frac{\partial v_0}{\partial \tilde{z}}\right) + \\ &\frac{3}{2}\lambda\frac{\mathrm{d}H}{\mathrm{d}\tilde{y}}\left(u_0^2+v_0^2\right)^{-1/4}\left(\frac{u_0}{H}\frac{\partial u_0}{\partial \tilde{z}} + \frac{v_0}{H}\frac{\partial v_0}{\partial \tilde{z}}\right)\Bigg) - \\ &\frac{\partial^2 \check{h}_1}{\partial \tilde{y}^2}\lambda\left(u_0^2+v_0^2\right)^{3/4}\Bigg) \quad \text{at } \tilde{z} = -1.\end{aligned} \tag{C5b}$$

In the equations above, we have written $\partial/\partial\tilde{x} = ik$ since the only x-dependency is in the form of $\exp(ikx)$, as shown in Equations 17 and 18.

Appendix D: Results for an Asymmetric Sand Bank

The asymmetric sand bank topography is defined by

$$H^*(y^*) = H_0^* - H_{\mathrm{sb}}^*\left(\frac{1}{2} + \frac{1}{2}\frac{\arctan\left(\frac{\mathcal{A}\sin(y^*+\varphi)}{1+\mathcal{A}\cos(y^*+\varphi)}\right)}{\arcsin(\mathcal{A})}\right)^n, \tag{D1}$$

where we have introduced the parameter $\mathcal{A}$, which represents the sand bank asymmetry, and the phase φ, which represents the position of the sand bank crest within the domain. Note that the limit $\mathcal{A} \to 0$ for $\varphi = -\pi/2$ yields the symmetric sand bank profile considered by default. Note that we have still considered an ambient symmetric tide, with a tidal ellipse that is deflected due to continuity and friction effects depending on the local depth.

The resulting sand wave topographies for the particular case with $\mathcal{A} = 0.7$ and $\varphi = -\pi/4$ are shown in Figure D1. The emerging sand waves on the steeper slope migrate faster than those on the milder slope

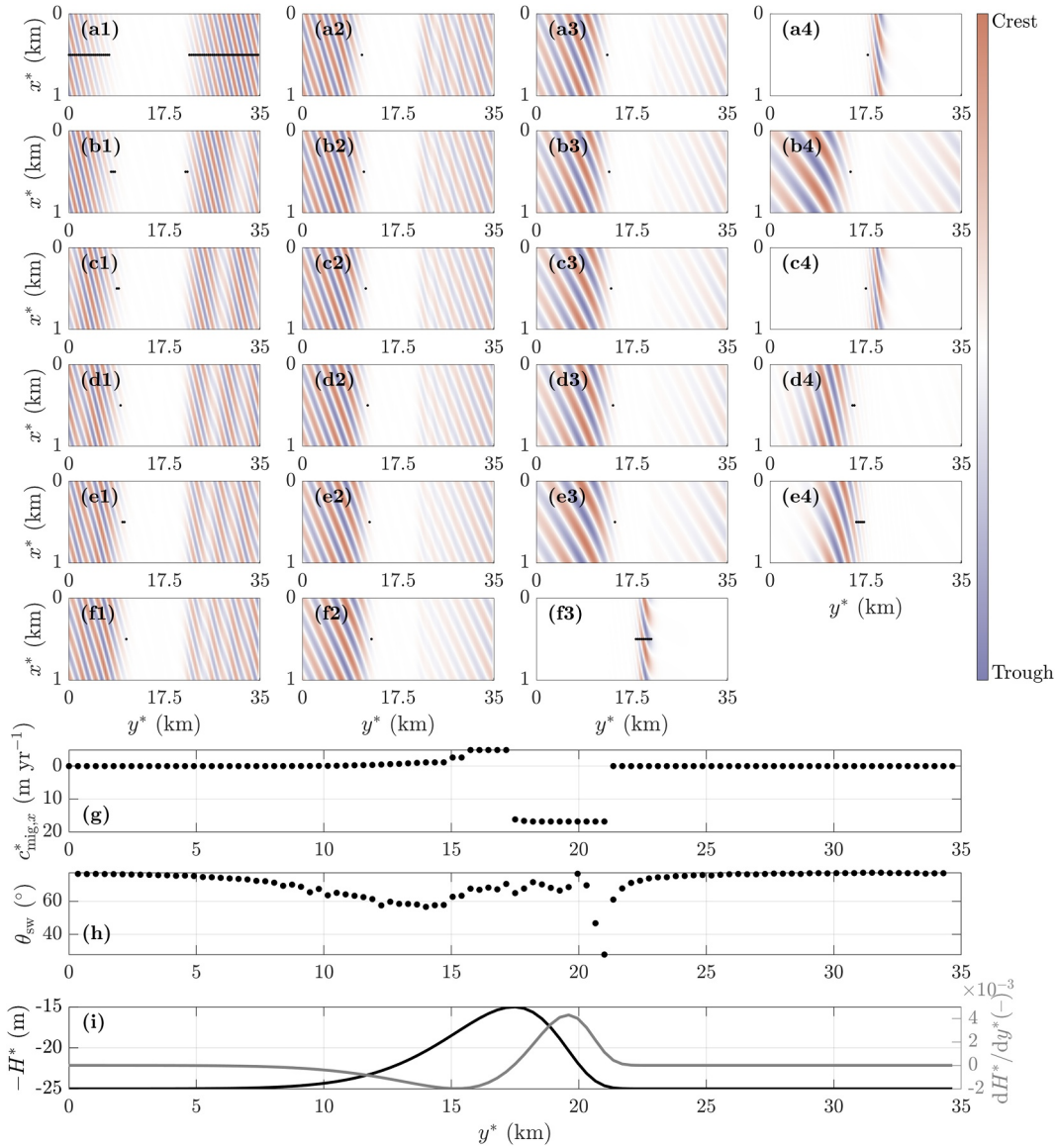

Figure D1. Same as Figure 6, but for an asymmetric sand bank, as specified in Equation D1. Note that the number of modes needed to give sand wave information over the entire domain is now 23.

(∼17 m yr^{-1} vs. ∼5 m yr^{-1}); and they are more oblique, reaching an angle of $\theta_{\mathrm{sw}} \sim 30°$. The ambient behavior (far from the sand bank) is similar to the symmetric sand bank case.

The case with an asymmetric tidal forcing would be more realistic than the symmetric tide considered here, but the lack of detailed observations on the M4 tidal constituents in the vicinity of a sand bank makes choosing representative model parameters difficult. Yet, we have run a case with a uniform M4 amplitude and phase across the sand bank, such that the basic flow corresponds to that of an asymmetric sand bank with milder slope on the left-hand side (such as that shown in Figure D1). Results (not shown here) show that main variations occur for the sand wave migration rates, being all more negative. Therefore, all sand waves migrate, also those on the sand bank flanks, and those on the sand bank crest have a less positive migration rate. An in-depth observational study or modeling study of how the M4 tidal constituent behaves in the vicinity of a sand bank is needed before we can further apply our model to such situations, which are beyond the scope of the present work.

Conflict of Interest

The authors declare no conflicts of interest relevant to this study.

Availability Statement

The MATLAB code for the basic state as well as the perturbed state solutions is available at the 4TU. ResearchData (Portos-Amill et al., 2025).

Acknowledgments
This work is part of the MELODY project (ModElling LOwer shoreface seabed DYnamics for a climate-proof coast, with project number 18949), funded by NWO, the Netherlands Organisation for Scientific Research. This work used the Dutch national e-infrastructure with the support of the SURF Cooperative using Grant EINF-13126. Laura Portos-Amill thanks Sem Geerts for insightful discussions on sand bank dynamics. We thank three anonymous reviewers for their feedback.

References

Besio, G., Blondeaux, P., Brocchini, M., Hulscher, S. J. M. H., Idier, D., Knaapen, M. A. F., et al. (2008). The morphodynamics of tidal sand waves: A model overview. *Coastal Engineering*, *55*(7), 657–670. https://doi.org/10.1016/j.coastaleng.2007.11.004

Borsje, B. W., Kranenburg, W. M., Roos, P. C., Matthieu, J., & Hulscher, S. J. M. H. (2014). The role of suspended load transport in the occurrence of tidal sand waves. *Journal of Geophysical Research: Earth Surface*, *119*(4), 701–716. https://doi.org/10.1002/2013JF002828

Calvete, D., Falqués, A., de Swart, H. E., & Walgreen, M. (2001). Modelling the formation of shoreface-connected sand ridges on storm-dominated inner shelves. *Journal of Fluid Mechanics*, *441*, 169–193. https://doi.org/10.1017/S0022112001004815

Caston, V. N. D. (1972). Linear sand banks in the Southern North Sea. *Sedimentology*, *18*(1–2), 63–78. https://doi.org/10.1111/j.1365-3091.1972.tb00003.x

Caston, V. N. D., & Stride, A. H. (1970). Tidal sand movement between some linear sand banks in the North Sea off northeast Norfolk. *Marine Geology*, *9*(5), M38–M42. https://doi.org/10.1016/0025-3227(70)90018-6

de Swart, H. E., & Yuan, B. (2019). Dynamics of offshore tidal sand ridges, a review. *Environmental Fluid Mechanics*, *19*(5), 1047–1071. https://doi.org/10.1007/s10652-018-9630-8

Dodd, N., Blondeaux, P., Calvete, D., de Swart, H. E., Falqués, A., Hulscher, S. J. M. H., et al. (2003). Understanding coastal morphodynamics using stability methods. *Journal of Coastal Research*, *19*(4), 849–865.

Dyer, K. R., & Huntley, D. A. (1999). The origin, classification and modelling of sand banks and ridges. *Continental Shelf Research*, *19*(10), 1285–1330. https://doi.org/10.1016/S0278-4343(99)00028-X

Hulscher, S. J. M. H. (1996). Tidal-induced large-scale regular bed form patterns in a three-dimensional shallow water model. *Journal of Geophysical Research*, *101*(C9), 20727–20744. https://doi.org/10.1029/96JC01662

Huthnance, J. M. (1973). Tidal current asymmetries over the Norfolk Sandbanks. *Estuarine and Coastal Marine Science*, *1*(1), 89–99. https://doi.org/10.1016/0302-3524(73)90061-3

Komarova, N. L., & Newell, A. C. (2000). Nonlinear dynamics of sand banks and sand waves. *Journal of Fluid Mechanics*, *415*, 285–321. https://doi.org/10.1017/s0022112000008855

Krabbendam, J., Nnafie, A., Borsje, B. W., & de Swart, H. E. (2023). Background topography affects the degree of three-dimensionality of tidal sand waves. *Journal of Geophysical Research: Earth Surface*, *128*(11), e2023JF007153. https://doi.org/10.1029/2023JF007153

Leenders, S., Damveld, J. H., Schouten, J., Hoekstra, R., Roetert, T. J., & Borsje, B. W. (2021). Numerical modelling of the migration direction of tidal sand waves over sand banks. *Coastal Engineering*, *163*, 103790. https://doi.org/10.1016/j.coastaleng.2020.103790

Loder, J. W. (1980). Topographic rectification of tidal currents on the sides of Georges Bank. *Journal of Physical Oceanography*, *10*(9), 1399–1416. https://doi.org/10.1175/1520-0485(1980)010⟨1399:TROTCO⟩2.0.CO;2

Loder, J. W., & Wright, D. G. (1985). Tidal rectification and frontal circulation on the sides of Georges Bank. *Journal of Marine Research*, *43*, 3–604. https://doi.org/10.1357/002224085788440367

Ma, X., Li, J., & Yan, J. (2018). Tide-induced bedload transport pathways in a multiple-sand-ridge system offshore of Hainan Island in the Beibu Gulf, northwest South China Sea. *Earth Surface Processes and Landforms*, *43*(13), 2738–2753. https://doi.org/10.1002/esp.4428

Németh, A. A., Hulscher, S. J. M. H., & De Vriend, H. J. (2003). Offshore sand wave dynamics, engineering problems and future solutions [Conference paper]. *Pipeline and Gas Journal*, *230*(4), 67–69.

Németh, A. A., Hulscher, S. J. M. H., & de Vriend, H. J. (2002). Modelling sand wave migration in shallow shelf seas. *Continental Shelf Research*, *22*(18), 2795–2806. https://doi.org/10.1016/S0278-4343(02)00127-9

Portos-Amill, L., Roos, P. C., Schuttelaars, H. M., & Hulscher, S. J. M. H. (2025). MATLAB code for local characteristics of sand wave patterns are governed by underlying sand bank: A linear stability approach [Software]. *4TU.ResearchData*. https://doi.org/10.4121/11EDB24D-904B-45E9-99C5-2CA35629B631.V1

Roos, P. C., Hulscher, S. J. M. H., Knaapen, M. A. F., & van Damme, R. M. J. (2004). The cross-sectional shape of tidal sandbanks: Modeling and observations. *Journal of Geophysical Research*, *109*(F2), F02003. https://doi.org/10.1029/2003JF000070

Trowbridge, J. H. (1995). A mechanism for the formation and maintenance of shore-oblique sand ridges on storm-dominated shelves. *Journal of Geophysical Research*, *100*(C8), 16071–16086. https://doi.org/10.1029/95JC01589

van den Eynde, D., Giardino, A., Portilla, J., Fettweis, M., Francken, F., & Monbaliu, J. (2010). Modelling the effects of sand extraction, on sediment transport due to tides, on the Kwinte Bank. *Journal of Coastal Research*, 101–116.

van der Meijden, R., Damveld, J. H., Ecclestone, D. W., van der Werf, J. J., & Roos, P. C. (2023). Shelf-wide analyses of sand wave migration using GIS: A case study on the Netherlands Continental Shelf. *Geomorphology*, *424*, 108559. https://doi.org/10.1016/j.geomorph.2022.108559

van der Spek, A., van der Werf, J. J., Oost, A., Vermaas, T., Grasmeijer, B., & Schrijvershof, R. (2022). The lower shoreface of the Dutch coast – An overview. *Ocean & Coastal Management*, *230*, 106367. https://doi.org/10.1016/j.ocecoaman.2022.106367

van Dijk, T. A. G. P., & Kleinhans, M. G. (2005). Processes controlling the dynamics of compound sand waves in the North Sea, Netherlands. *Journal of Geophysical Research*, *110*(F4), F04S10. https://doi.org/10.1029/2004JF000173

van Landeghem, K. J., Baas, J. H., Mitchell, N. C., Wilcockson, D., & Wheeler, A. J. (2012). Reversed sediment wave migration in the Irish Sea, NW Europe: A reappraisal of the validity of geometry-based predictive modelling and assumptions. *Marine Geology*, *295–298*, 95–112. https://doi.org/10.1016/j.margeo.2011.12.004

van Rijn, L. C. (1993). Bed material suspension and transport in steady uniform currents. In *Principles of sediment transport in rivers, estuaries and coastal seas*. Aqua Publications.

Zhou, J., Wu, Z., Zhao, D., Guan, W., Cao, Z., & Wang, M. (2022). Effect of topographic background on sand wave migration on the eastern Taiwan Banks. *Geomorphology*, *398*, 108030. https://doi.org/10.1016/j.geomorph.2021.108030